JACS
JOURNAL OF THE AMERICAN CHEMICAL SOCIETY
pubs.acs.org/JACS
Article

Mechanism of Giant Magnetic Field Effect in a Red Fluorescent Protein

Katherine M. Xiang, Hana Lampson, Rebecca Frank Hayward, Andrew G. York, Maria Ingaramo, and Adam E. Cohen*

Cite This: *J. Am. Chem. Soc.* 2025, 147, 18088−18099

Read Online

ACCESS | Metrics & More | Article Recommendations | Supporting Information

ABSTRACT: Several fluorescent proteins, when expressed in *E. coli*, are sensitive to weak magnetic fields. We found that mScarlet3 fluorescence in *E. coli* reversibly decreased by 21% in the presence of a 60 mT magnetic field, the largest magnetic field effect (MFE) reported in any fluorescent protein. Purified mScarlet3 did not show an MFE, but the addition of flavin mononucleotide (FMN) and simultaneous illumination with blue and yellow light restored the MFE. Through extensive photophysical experiments, we developed a quantitative model of the giant MFE in mScarlet3-FMN mixtures. The key reaction step involved electron transfer from fully reduced $FMNH_2$ to triplet-state mScarlet3 to form a triplet spin-correlated radical pair. The magnetic field then controlled the branching ratio between singlet recombination vs triplet separation. Our quantitative model of the mScarlet3-FMN photocycle provides a framework for the design and optimization of magnetic-field-sensitive proteins, opening possibilities in fluorescent protein-based magnetometry, magnetic imaging, and magnetogenetic control.

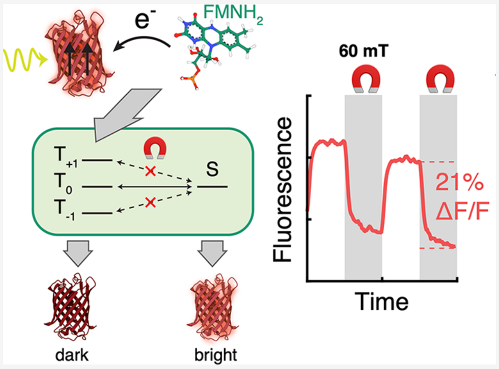

INTRODUCTION

Interactions between milli-Tesla magnetic fields and organic matter at room temperature are too weak to affect reaction outcomes through thermodynamic means. Nonetheless, magnetic field effects (MFEs) on photochemical reactions have long been observed in organic dye solutions[2−5] and in some biochemical systems, but such effects are typically small (<1%)[6,7] or restricted to nonphysiological conditions.[8,9] Identification of large (>10%) MFEs in biochemical reactions under physiological conditions would open the possibility to harness these effects to modulate biochemical signals, or to implement quantum coherent measurement or control protocols in biology, and may shed light on possible mechanisms of magnetosensation.

A recent report described MFEs in several fluorescent proteins in live *E. coli*, and when paired with redox cofactors in vitro.[1] Enhanced green fluorescent protein (EGFP) fused to a flavin-binding tag showed a 0.25% MFE in *E. coli* when exposed to a 25 mT field. A mixture of purified mScarlet, a red fluorescent protein, and FMN showed a nearly 3% MFE in a 10 mT magnetic field, provided that the sample had been preilluminated with 470 nm light. Mutagenesis and screening in a light-oxygen-voltage-sensing (LOV) domain protein led to an astonishing 35% magnetic modulation in flavin fluorescence in an engineered variant termed magLOV.[1] The mechanisms underlying these newly discovered MFEs are not known.

MFEs are thought to arise through quantum dynamics in a spin-correlated radical pair intermediate (reviewed extensively in ref 10). Briefly, an electronic excited state — usually produced by photoexcitation — undergoes electron transfer to produce a pair of electrons that are weakly interacting but whose spin states are in a nonthermal distribution, favoring either singlet or triplet states, i.e. a spin-correlated radical pair (SCRP). Each electron spin precesses under the influence of distinct hyperfine interactions with nearby nuclear spins, leading to interconversion between singlet and triplet states, known as intersystem crossing (ISC). An external magnetic field partially decouples the electron and nuclear spins, suppressing ISC. Singlet radical pairs are more likely to recombine, while triplets are more likely to separate, leading to an MFE on the photochemical reaction outcome.

While the broad outlines of the SCRP mechanism are well established, the molecular species, reaction steps, and rate constants were not known for the MFE in any fluorescent protein. In particular, the reported requirement for preillumination with blue light in the mScarlet/FMN MFE was a

Received: March 8, 2025
Revised: May 7, 2025
Accepted: May 8, 2025
Published: May 15, 2025

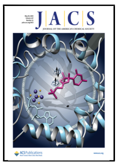

https://doi.org/10.1021/jacs.5c03997
J. Am. Chem. Soc. 2025, 147, 18088−18099

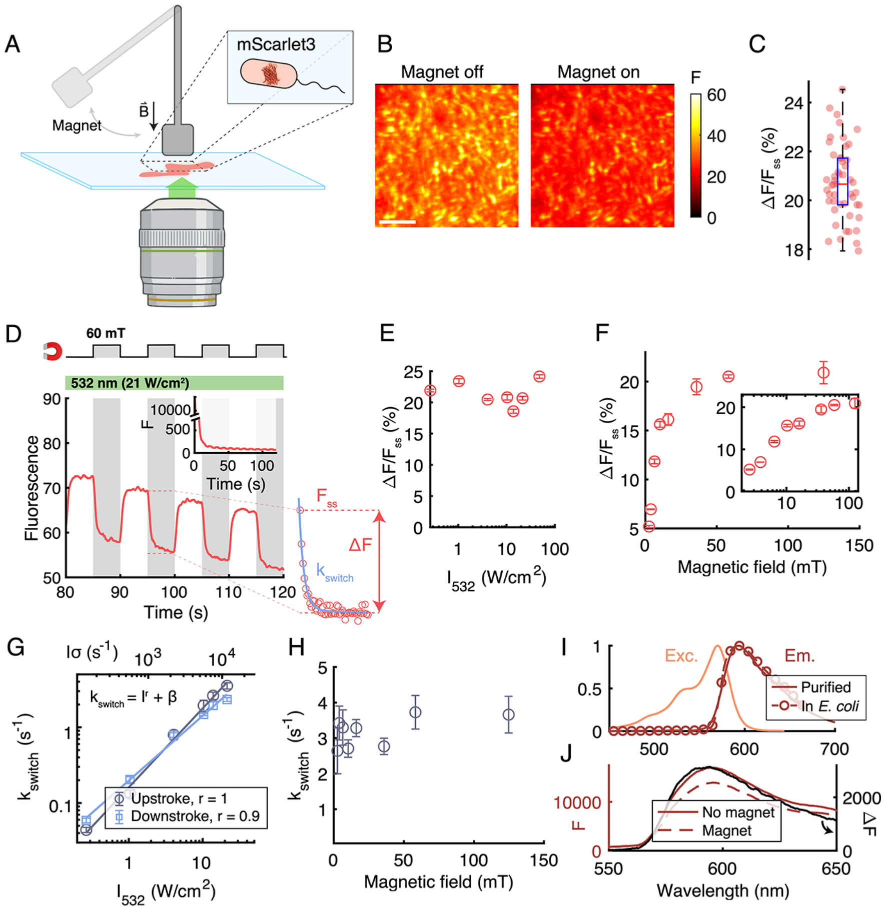

Figure 1. mScarlet3 fluorescence in *E. coli* is magnetic field sensitive. (A) Experimental setup. Fluorescence of *E. coli* expressing mScarlet3 (PDB ID: 7zct)[49−51] was probed via epifluorescence microscopy, while a magnet on a servo modulated the local magnetic field. (B) Image of *E. coli* expressing mScarlet3 in the absence (left) or presence (right) of a 60 mT magnetic field. Same contrast for both images. Scale bar 10 μm. (C) Distribution of amplitudes of the MFE across individual *E. coli*. $\Delta F/F_{ss} = (20.7 \pm 1.5)\%$ (mean ± s.d., $n = 50$ cells). Boxplot shows median, 25th and 75th percentiles; whiskers show extrema. (D) Fluorescence time-trace of mScarlet3 under green excitation (532 nm, 21 W/cm^2) and alternating magnetic field. Inset: upon illumination onset, fluorescence rapidly quenched. Right: definitions of the parameters k_{switch}, ΔF, and F_{ss}. (E) Steady state MFE amplitude as a function of illumination intensity. Magnetic field was 60 mT. (F) Steady state MFE amplitude as a function of magnetic field. Illumination intensity was 21 W/cm^2. (G) Switching rate as a function of illumination intensity. Magnetic field was 60 mT. Rates were approximately first-order in illumination intensity for both the upstroke and the downstroke. (H) MFE switching rate for the upstroke as a function of magnetic field. Illumination intensity was 21 W/cm^2. Rates were independent of magnetic field. (I) Excitation and emission spectra of purified mScarlet3 (solid curve), overlaid with emission spectrum of *E. coli* expressing mScarlet3 (circles). (J) Magnetic field modulated the amplitude (red traces), but not the shape (black trace), of the fluorescence emission spectrum. Error bars for E−H denote s.e.m.

mystery. In a previous report on an MFE involving flavin and proteins, the photoexcited flavin oxidized the protein.[7] In the mScarlet3/FMN system, we find that photochemically produced FMNH$_2$ reduces the protein. The MFE photocycle provides a guide for efforts to apply or enhance protein-based magnetic field effects and for coherent control of spin dynamics in proteins.

■ RESULTS

mScarlet3 Shows a Large MFE in Live *E. coli*. We imaged the fluorescence of several red fluorescent proteins expressed in live *E. coli* using an epifluorescence microscope. We used a servo-controlled permanent magnet on a stick to switch the magnetic field between 0 and 60 mT (Figure 1A). We tested red-emitting fluorescent proteins mScarlet3, mScarlet-I3, mSandy2, mRuby3, and mKate2. All except mKate2 showed magnetically modulated fluorescence (Figure S1).

We focused on mScarlet3 because it was bright and had the largest MFE of the proteins we tested. In the presence of the magnetic field ($B = 60$ mT), the fluorescence of mScarlet3 was visibly dimmer than in its absence (Figure 1B; 532 nm excitation, 48 W/cm^2, 575 nm long-pass emission, B switching every 5 s). We quantified the MFE amplitude by $\Delta F/F_{ss}$, where F_{ss} is the steady-state fluorescence at magnetic field $B = 0$, and $\Delta F = F_{ss} - F(B)$. Quantification across individual mScarlet3-expressing bacteria showed an MFE of $\Delta F/F_{ss} = 20.7 \pm 1.5\%$ (mean ± s.d., $n = 50$ cells, Figure 1C).

We then explored how the illumination intensity and the magnetic field strength affected the dynamics of the fluorescence. Upon onset of illumination at 21 W/cm^2, the fluorescence rapidly quenched from 13,000 to 80 counts, with a time-constant of ~1.8 s (Figure 1D inset). After the fluorescence stabilized, stepwise changes in magnetic field induced gradual changes in fluorescence. The steady-state MFE amplitude was independent of the excitation intensity over the measured range $I = 0.3$−48 W/cm^2 (Figures 1E and

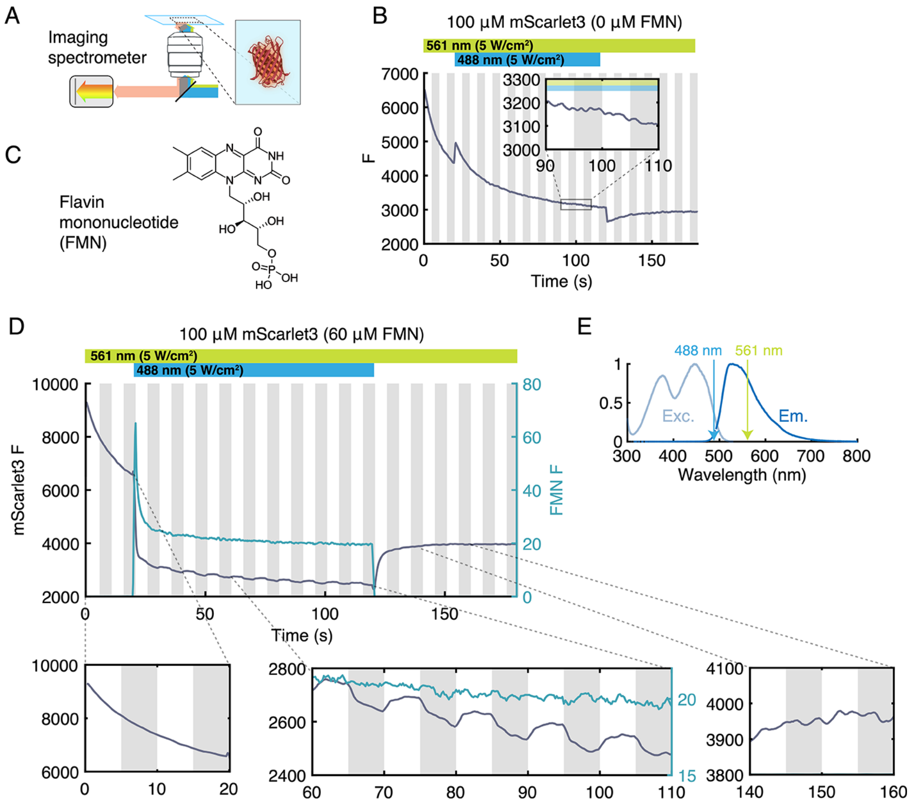

Figure 2. The mScarlet3 MFE requires FMN and blue light. (A) Fluorescence spectra were measured in a microscope with an imaging spectrometer. (B) Fluorescence of purified mScarlet3 showed no MFE under yellow (561 nm) or yellow + blue (488 nm) illumination. The magnetic field was modulated in 5 s intervals between $B = 60$ mT (gray stripes) and $B = 0$ (white stripes). (C) Chemical structure of FMN. (D) Addition of FMN (60 μM) did not affect mScarlet3 fluorescence under yellow-only illumination. Onset of blue illumination led to partial quenching of mScarlet3 fluorescence and appearance of an MFE. Fluorescence was spectrally filtered to separately record mScarlet3 and flavin emission. (E) Excitation and fluorescence emission spectra of FMN.

S2). The steady-state MFE amplitude increased with increasing magnetic field, with a half-saturation field $B_{1/2} = 5.5$ mT (Figure 1F).

We fit the magnetic field-induced switching rate constant, k_{switch} (defined in Figure 1D), over an intensity range from $I = 0.3\text{−}21$ W/cm^2 (corresponding to per-molecule excitation rates $I\sigma = 145\text{−}11{,}600$ s^{-1}; σ is the absorption cross-section at 532 nm and is proportional to $\varepsilon_{532} = 53{,}040$ M^{-1} cm^{-1}). The switching rate at magnetic field onset varied from 0.04 to 3.5 s^{-1} over this range, and was approximately linear in intensity, i.e., $k_{\text{switch}} \propto I^r + \beta$ with $r = 1.0$ for the fluorescence upstroke and $r = 0.9$ for the downstroke (Figure 1G). These results suggested a single rate-limiting photochemical step in the magnetic-field dependent photochemical reaction. The ratio of k_{switch} (s^{-1}) to per-molecule excitation rate $I\sigma$ (s^{-1}) gives a branching ratio of 3.1×10^{-4} for magnetic field-dependent photoswitching from bright to dark forms of mScarlet3.

The switching rate was independent of the magnetic field strength over the range 3−125 mT (Figure 1H), implying that the magnetically modulated rate constant(s) were not the rate-limiting steps in the photochemical conversion between fluorescent and non-fluorescent mScarlet3 states. The fluorescence emission spectrum of the *E. coli* closely matched the spectrum for purified mScarlet3 (Figure 1I),[11] and the MFE modulated the amplitude, but not the shape, of this spectrum (Figure 1J). These observations indicate that mScarlet3 was the primary emissive species.

In *E. coli*, various factors could influence the MFE including pH, redox factors, and diffusional confinement of molecules within each bacterium. We found that the MFE was largest on the second day of expression in liquid culture, suggesting the involvement of metabolic or redox factors beyond just the fluorescent protein. To study the molecular mechanisms underlying the MFE under controlled conditions, we thus switched to working with purified protein.

Purified mScarlet3 Shows an MFE in the Presence of FMN and Blue Light. We purified mScarlet3 and measured its fluorescence while varying the magnetic field. An imaging spectrometer recorded both the amplitude and shape of the emission spectrum (Figure 2A). No MFE was detected for yellow (561 nm) or yellow + blue (561 + 488 nm) excitation (Figure 2B). Prior work showed that the addition of flavin mononucleotide (FMN, Figure 2C) and blue light restored the MFE in mScarlet3,[1] so we replicated that result. Addition of 60 μM FMN did not produce an MFE under yellow light alone. However, when we combined blue and yellow light in the presence of FMN, we observed a rapid initial drop in mScarlet3 fluorescence, and then an MFE (Figure 2D). The blue light also evoked FMN fluorescence, which was spectrally distinct from mScarlet3 fluorescence. The FMN fluorescence showed a rapid initial drop before stabilizing, but did not show a detectable MFE. Upon turning off the blue light, the mScarlet3 fluorescence partially recovered, and the MFE went away.

Based on these measurements, and the overlap of the blue laser wavelength with the FMN absorption spectrum (Figure 2E), we speculated that a photochemical product of FMN excitation might be involved in the MFE. To test this hypothesis, we prepared a sample comprising mScarlet3 immobilized on Ni-NTA resin beads, immersed in a solution of FMN (500 μM), and sandwiched between glass coverslips. We targeted the yellow light to focus on a single bead, and the blue light to pass through a region of FMN solution approximately 200 μm from the bead (Figure 3A,B). This arrangement prevented any direct blue light interaction with mScarlet3 molecules, while allowing diffusive interchange of long-lived photoproducts between the two illuminated regions. We measured the emission from both the blue-illuminated and yellow-illuminated regions with an imaging spectrometer (Figure 3B, right), while we varied the magnetic field.

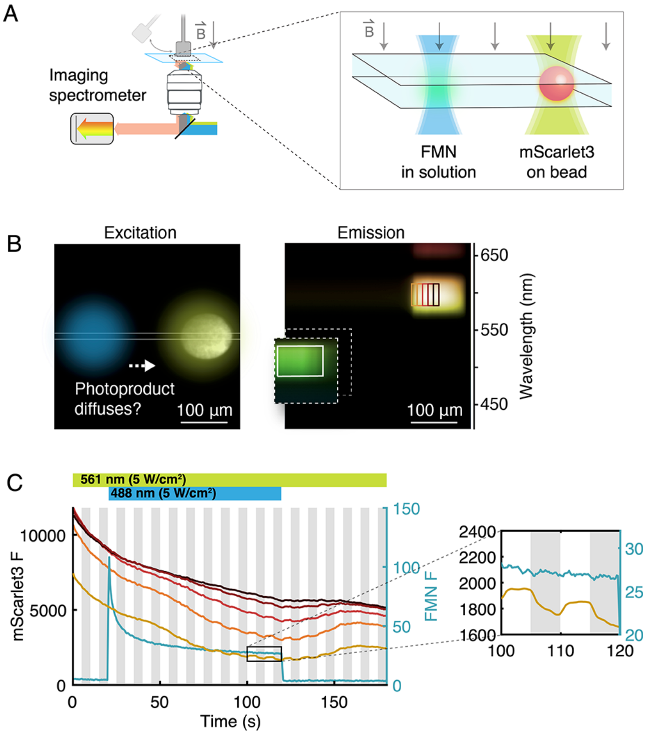

Figure 3. The mScarlet3 MFE requires a long-lived FMN photoproduct. (A) Experiment to test whether an FMN photoproduct contributed to the MFE. A bead containing tethered mScarlet3 was illuminated with yellow light. Blue light was laterally displaced and focused into a solution of FMN. (B) Left: excitation profiles overlaid on an image of the bead. Right: emission of FMN (green) and mScarlet3 (yellow) on an imaging spectrometer. The *x*-axis corresponds to position and the *y*-axis to emission wavelength. The contrast of the FMN emission has been increased to render it visible. (C) Time-course of FMN fluorescence (cyan) and mScarlet3 fluorescence in the regions on the bead indicated with correspondingly colored rectangles in (B). The magnetic field was modulated in 5 s intervals between $B = 60$ mT (gray stripes) and $B = 0$. Approximately 35 s after blue light onset, the mScarlet3 fluorescence showed quenching and onset of an MFE, with the regions closer to the blue light responding first. The FMN fluorescence was not detectably magnetic field sensitive.

As with the soluble proteins, the mScarlet3 initially showed no MFE under yellow-only illumination. When the blue light was turned on, the FMN fluorescence decayed over ~15 s, suggesting photochemical consumption of the FMN. As before, there was no detectable MFE in the FMN fluorescence. After a delay of ~35 s, the mScarlet3 fluorescence began to drop, and an MFE appeared (Figure 3C). The side of the bead closest to the blue spot had the earliest and largest response, and more distant regions had later and smaller responses. When the blue light was turned off, the MFE persisted for ~35 s, and then gradually faded as the mScarlet3 fluorescence recovered.

These experiments taught us several important facts. First, they established that a relatively long-lived FMN photoproduct was necessary for the MFE. Second, the magnet did not act on the blue-mediated FMN photochemistry, but rather on the interaction of the FMN photoproduct with yellow-excited mScarlet3. Third, the MFE did not require blue light interaction with mScarlet3 itself (or with mScarlet3 photoproducts). We estimated the diffusion coefficient of the FMN photoproduct from $D \approx x^2/2t$, where $x = 200$ μm was the distance between the blue laser spot and the mScarlet3-labeled bead, and $t = 35$ s was the delay between blue illumination and onset of the MFE. This estimate gave $D \approx 570$ $\mu m^2/s$, broadly consistent with diffusion of a small molecule in water (due to the complex geometry, this estimate for D is likely only accurate within a factor of ~2).

mScarlet3 MFE Requires Both Oxidized and Reduced FMN. Optically excited FMN is a potent oxidizing agent, readily forming the semiquinone radical. In the absence of an exogenous electron donor, the ribityl chain of another FMN molecule donates an electron.[12,13] The semiquinone radical spontaneously disproportionates to re-form FMN and the doubly reduced $FMNH_2$ (Figure 4A).[13−17] We speculated that photochemically produced $FMNH_2$ might mediate the MFE.

To test this hypothesis, we produced $FMNH_2$ by illuminating FMN (3.3 mM) with high intensity 488 nm light (60 W/cm^2), in a solution also containing mScarlet3 (100 μM). As before, we used yellow light (561 nm, 10 W/cm^2) to probe the mScarlet3 fluorescence. To our surprise, the mScarlet3 fluorescence rapidly quenched to almost zero, and the MFE was initially not detectable (Figure 4B). This observation seemed to contradict our hypothesis. However, after the blue light was turned off, the fluorescence gradually increased, and the MFE appeared, growing proportionally with the fluorescence. We hypothesized that the FMN concentration increased during this interval via a combination of reoxidation of $FMNH_2$ by ambient oxygen and diffusion of FMN from the nonilluminated regions of the sample into the observation region; and that perhaps it was necessary to have both $FMNH_2$ and FMN in the solution to observe the MFE.

To test this revised hypothesis, we produced $FMNH_2$ by illuminating FMN with 488 nm light in the presence of 5 mM ethylenediaminetetraacetic acid (EDTA), an efficient electron donor for photoreduction of FMN.[13,16,18] We performed the photoreduction in an anaerobic glovebox to avoid reoxidation. Absorption spectra confirmed photoreduction of FMN to $FMNH_2$ (Figure 4C). We then prepared mixtures with degassed solutions containing well-defined concentrations of $FMNH_2$, FMN, and mScarlet3 under anaerobic conditions (Figure 4D), and sealed the samples for characterization.

We used a home-built apparatus to interleave measurements of the absorption and fluorescence emission spectra while exciting the mScarlet3 with yellow light and varying the magnetic field (Figure 4E). In a sample of 30 μM $FMNH_2$ and 6 μM mScarlet3 (and no FMN), illumination with 561 nm light (1.7 W/cm^2) caused a rapid quenching of the mScarlet3

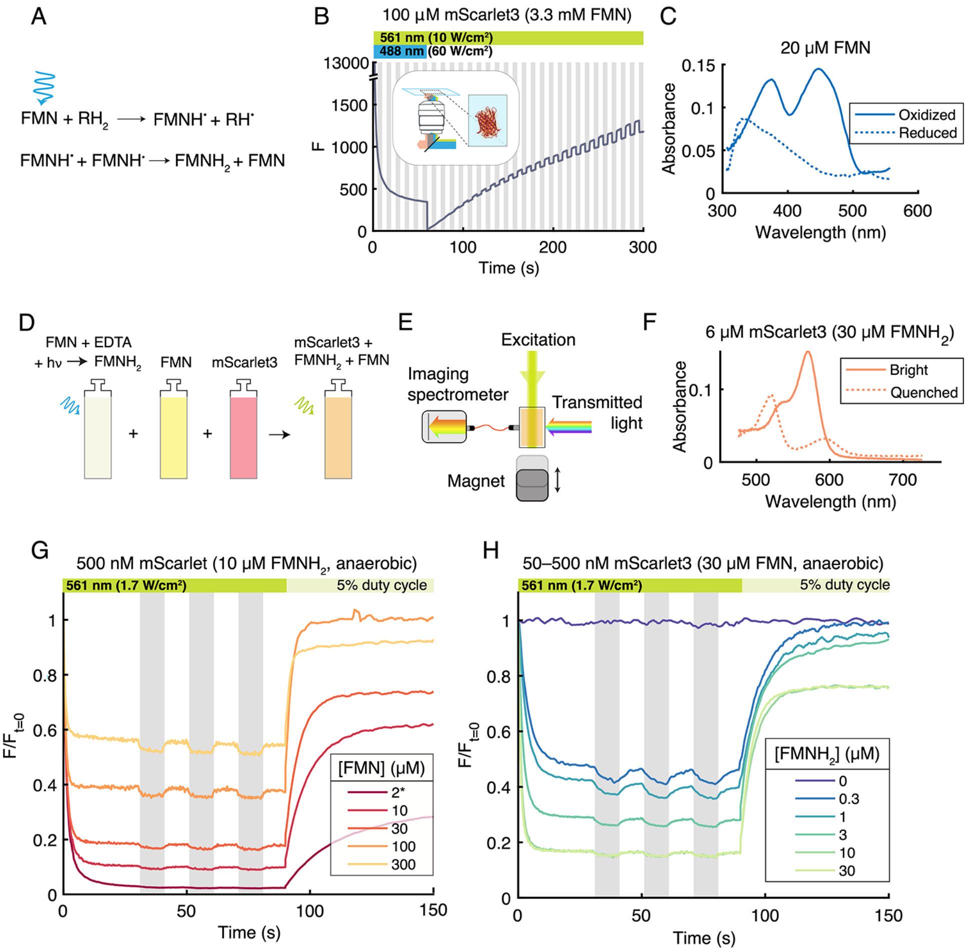

Figure 4. The mScarlet3 MFE requires both oxidized and reduced FMN. (A) Photoexcitation of FMN produces FMNH$_2$. (B) Fluorescence of purified mScarlet3 with an excess of FMN and high-intensity blue light. The fluorescence quenched almost completely (residual fluorescence during blue illumination is the tail of the FMN emission and autofluorescence due to the high blue intensity). Upon turning off the blue light, the mScarlet3 fluorescence recovered and the MFE increased proportionally. (C) Absorption spectra of FMN in its oxidized and photoreduced (FMNH$_2$) states. (D) Samples of FMNH$_2$, FMN, and mScarlet3 were prepared separately in anaerobic conditions, and then combined and measured under 561 nm illumination. (E) Top view of the experimental apparatus. Magnetic field-dependent fluorescence and absorption spectra were recorded on a spectrometer. (F) Absorption spectra of mScarlet3 and the fully photoreduced mScarlet3 product (presumably mScarlet3$^{\cdot-}$ radical anion) in the presence of FMNH$_2$. (G, H) mScarlet3 fluorescence quenching, MFE, and recovery in samples with indicated concentrations of FMN and FMNH$_2$. All fluorescence traces are normalized to their initial value. A 5% duty cycle of yellow light (25 ms every 0.5 s) was used to image the fluorescence recovery. Fluorescence during this epoch was scaled 20× to account for the lower illumination intensity. Asterisk indicates FMN concentration determined from absorption measurements (Experimental Section; Figure S3).

fluorescence to almost zero. The absorption spectrum of the mScarlet3 photoproduct was distinct from unquenched mScarlet3 (Figure 4F) with both a blue-shifted and red-shifted peak. We ascribe this spectrum to a photoreduction of mScarlet3 by FMNH$_2$, most likely to form the mScarlet3$^{\cdot-}$ radical anion. The putative mScarlet3$^{\cdot-}$ radical anion was not fluorescent under 561 nm excitation.

We then systematically varied the concentrations of FMN and FMNH$_2$ in mScarlet3 solutions and recorded the magnetic field-dependent fluorescence (Figure 4G,H). When [FMNH$_2$] was 1 μM or less, we used 50 nM mScarlet3 to ensure that FMNH$_2$ was in excess; otherwise, we used 500 nM mScarlet3. Complete photoreduction from FMN to FMNH$_2$ is difficult,[19] so for the samples with low [FMN] we determined the concentrations of each flavin species from absorption spectra (Figure S3). In contrast to previous experiments, the MFE only required yellow light.

Increasing [FMNH$_2$] decreased the steady-state mScarlet3 fluorescence, and increasing [FMN] counteracted this effect. The MFE was largest in absolute magnitude when these two effects were balanced so the steady-state fluorescence was approximately half its initial value. At fixed [FMNH$_2$], increasing [FMN] increased the rate of initial quenching and also the rate of magnetic field-induced switching (Figure 4G). In the absence of FMNH$_2$, FMN had no effect on mScarlet3 and did not induce an MFE (Figure 4H, purple trace), as we observed previously (e.g., Figure 2B).

After 90 s of yellow illumination, we decreased the yellow intensity to 5% (85 mW/cm^2), to monitor the recovery of mScarlet3 fluorescence in close-to-dark conditions. The rate of mScarlet3 recovery in dim yellow light depended on [FMN] and was largely independent of [FMNH$_2$] (except for the small effect of residual yellow-light + FMNH$_2$-mediated quenching).

In anaerobic conditions, the MFE persisted overnight (Figure S4A), establishing that the active FMN photoproduct was stable in the absence of oxygen, while stirring the solution in air immediately abolished the MFE. All evidence was consistent with FMNH$_2$ as the photoproduct responsible for

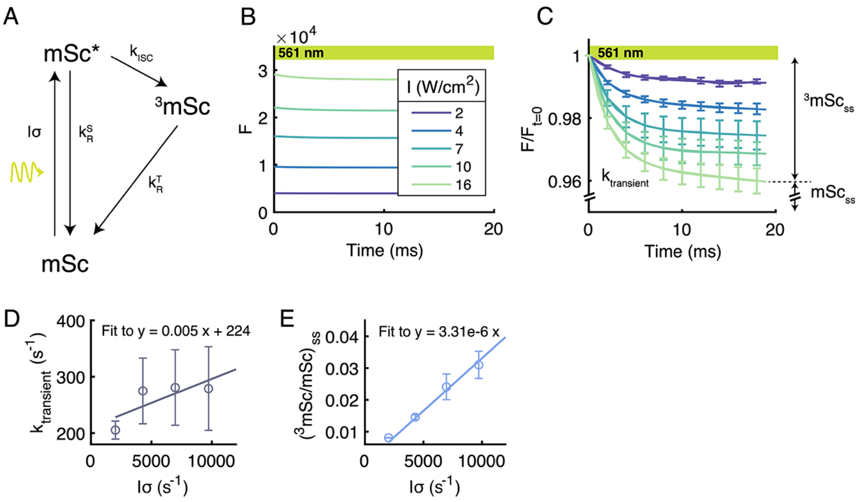

Figure 5. Illumination of mScarlet3 populates a transient dark state. (A) Three-state model of intersystem crossing (ISC) in mScarlet3. (B) Onset of high-intensity illumination of mScarlet3 immobilized on an agarose Ni-NTA bead induced a rapid and reversible slight decrease in fluorescence. (C) Data from (B), normalized to initial fluorescence, with exponential + linear fits. More intense illumination led to a larger fractional decrease in fluorescence. The relative amplitudes of the fluorescence dip and the fluorescence steady-state correspond to the relative triplet and ground-state populations (assuming negligible singlet excited state population). Traces are averaged over 18 flashes for each of $n = 3$ beads. Fitting the (D) rate constant and (E) amplitude of the fluorescence dip implied $k_R^T \approx 224$ s^{-1} and $k_{ISC} \approx 1.9 \times 10^5$ s^{-1}. Error bars denote s.e.m.

photoinduced mScarlet3 quenching and the MFE. To rule out the possibility of species other than $FMNH_2$ and FMN contributing to the MFE, we tested mixtures of mScarlet3 with EDTA alone (Figure S4B), as well as with FMN photoproducts lumichrome and H_2O_2 (Figure S4C).[13,17,18] None of these mixtures showed an MFE. We measured the MFE at several pH values to determine whether the reductant was $FMNH_2$ or $FMNH^-$, as $FMNH_2$ has a pK_a of 6.7.[19] The mScarlet3 fluorescence quenched more at lower pH, suggesting that $FMNH_2$ was the relevant species (Figure S5).

Together, these results imply that $FMNH_2$ electrochemically reduced the optically excited mScarlet3 to form a nonfluorescent protein photoproduct, and FMN reoxidized this photoproduct to reform ground-state mScarlet3. In this model, electron transfer from $FMNH_2$ to mScarlet3 likely proceeded through a radical-pair intermediate, whose branching between recombination and separation was magnetic field sensitive.

mScarlet3 Photoreduction Likely Proceeds through an mScarlet3 Triplet State. Two observations led us to suspect that $FMNH_2$ electrochemically reduced photogenerated mScarlet3 triplet (^{3}mSc) rather than the excited mScarlet3 singlet (mSc*). First, under our illumination conditions, the population of mSc* was very low. The mSc* lifetime is 4 ns,[11] and at an excitation intensity of 1.7 W/cm^2 at 561 nm, the per-molecule excitation rate was $I\sigma = 1652$ s^{-1} ($\varepsilon_{561} = 90{,}480$ M^{-1} cm^{-1}). Thus, the excited-state to ground-state ratio mSc*/mSc $\approx 6 \times 10^{-6}$. At 10 μM $FMNH_2$, and a measured rate of initial quenching of 0.98 s^{-1}, the implied bimolecular rate constant if the reaction proceeded from mSc* would be 8.3×10^{10} M^{-1} s^{-1}, substantially greater than the diffusion-limited aqueous bimolecular rate constant, 6.6×10^9 M^{-1} s^{-1}.[20] Hence a reaction from a long-lived triplet which could accumulate to higher concentration was more likely.

Second, we noted that the magnet decreased the mScarlet3 fluorescence. A magnetic field prolongs the lifetime of the initial spin state of a SCRP. A singlet SCRP is more likely to recombine, releasing ground-state mScarlet3, which can fluoresce, while a triplet SCRP is more likely to diffusively separate, building up a population of non-fluorescent $mSc^{\cdot -}$ radical anion. Thus, we surmised that the SCRP was likely born in a triplet state. The electron-transfer reaction usually conserves spin, so one of the reactants was likely a triplet. $FMNH_2$ has a singlet ground state, so the mScarlet3 was likely in a triplet state.

We measured the mSc* → ^{3}mSc intersystem crossing and ^{3}mSc → mSc recovery rates for mScarlet3 (with no flavin or other redox factors present), which we modeled as a three-state system (Figure 5A). In an anaerobic sample of mScarlet3 bound to beads (to eliminate effects of diffusion), we applied pulses of 561 nm light at different intensities (Figure 5B) and recorded the millisecond-time scale fluorescence dynamics (Figure 5C). We observed a reversible intensity-dependent initial dip in the fluorescence, which we attributed to populating the mScarlet3 triplet state. We quantified the rate (Figure 5D) and amplitude (Figure 5E) for this initial dip as a function of the mScarlet3 excitation rate ($I\sigma$), where I is the excitation intensity (photons/cm^2/s) and σ is the absorption cross section at 561 nm (cm^2). From these, we determined $k_R^T \approx 224$ s^{-1} and $k_{ISC} \approx 1.9 \times 10^5$ s^{-1} (Supporting Information).

Quantitative Model of the mScarlet3/$FMNH_2$/FMN Magnetic Field Effect. Combining all the above results, we developed a model of the mScarlet3 and FMN magnetic field effect (Figure 6A). In a solution initially containing only FMN, the blue illumination produced $FMNH_2$. Alternatively, the $FMNH_2$ can be produced separately and added to the solution under anaerobic conditions. Yellow excitation populated the mScarlet3 triplet state (^{3}mSc, Figure 5). In the key reaction step, $FMNH_2$ donated an electron to the mScarlet3 triplet state, producing an initially triplet spin-correlated radical pair, $^3[mSc^{\cdot -} + FMNH^{\cdot}]$. The magnetic field suppressed intersystem crossing to the singlet. The radical pair either recombined (more likely if in a singlet) or separated (more likely if in a triplet). Once separated, FMN reoxidized $mSc^{\cdot -}$ back to mScarlet3. This model contrasts with the MFE in interactions of FMN with a non-fluorescent protein backbone, where the optically excited FMN is proposed to accept an electron from the protein to produce a SCRP.[7]

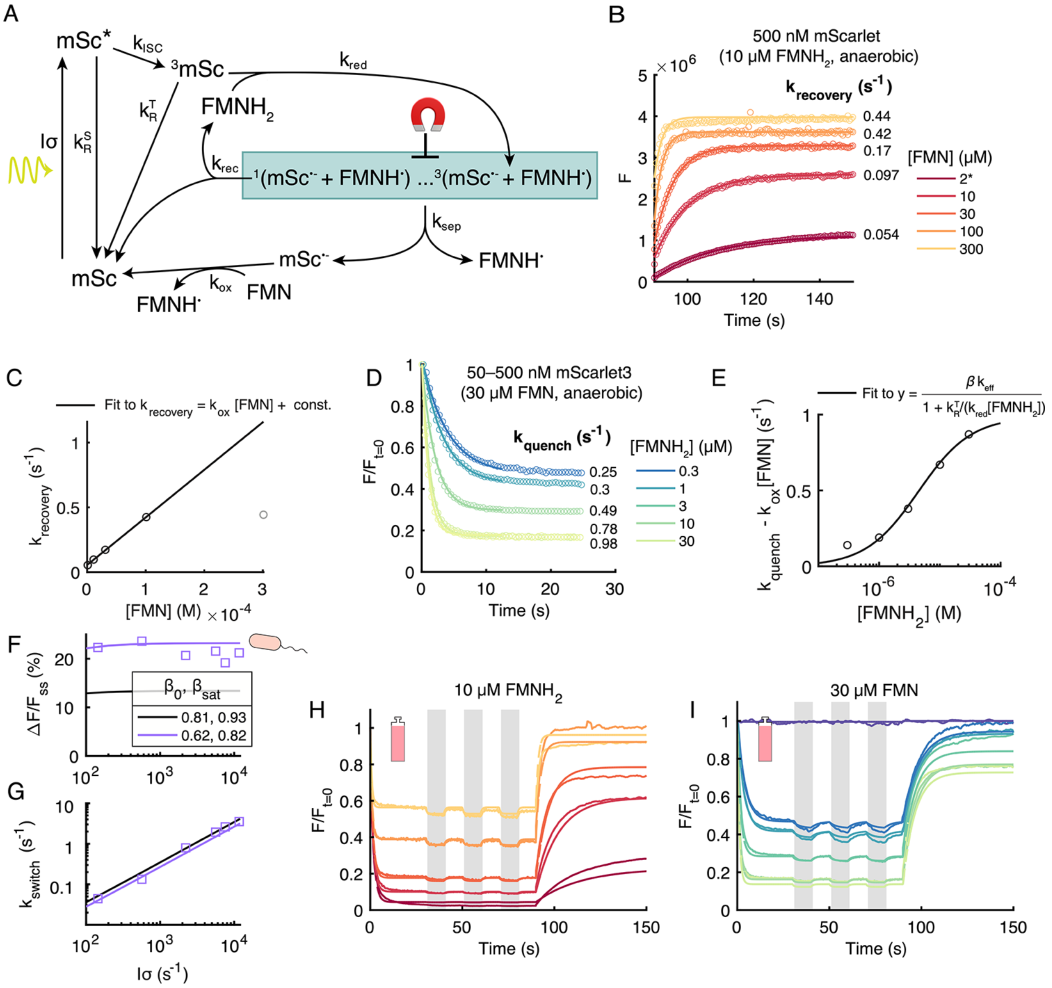

Figure 6. Quantitative model of giant MFE in mixture of mScarlet3, FMN, and $FMNH_2$. (A) Proposed mechanism. A yellow photon excites mScarlet3. The excited singlet state either fluoresces or undergoes ISC to produce the mScarlet3 triplet. Blue light drives photoreduction of FMN to $FMNH_2$ (reactions shown in Figure 4A). $FMNH_2$ donates an electron to triplet mScarlet3 to form a triplet-born spin-correlated radical pair (SCRP). The magnetic field controls the rate of ISC in the SCRP. Singlet products preferentially recombine to reform ground-state mScarlet3. Triplet products diffuse apart to release a non-fluorescent mScarlet3$^{\cdot-}$ radical anion. FMN reoxidizes the mScarlet3$^{\cdot-}$ back to the mScarlet3 ground state. (B) Exponential + constant fits of the fluorescence recovery for the FMN titration in Figure 4G. (C) Linear fit of k_{recovery} as a function of [FMN] determines the rate constant k_{ox} of mScarlet3$^{\cdot-}$ reoxidation by FMN. (D) Exponential + constant fits of the fluorescence quenching for the $FMNH_2$ titration in Figure 4H. (E) Fitting k_{quench} as a function of [$FMNH_2$] determines parameters β_0 and k_{red} (Supporting Information). (F) Comparison of measured and predicted MFE amplitude as a function of light intensity in *E. coli*. (G) Comparison of measured and predicted MFE upstroke switching rate as a function of light intensity in *E. coli*. (H, I) Comparison of measured and predicted fluorescence dynamics for the experiments in Figures 4G,H. All rate constants in (F–I) were identical. The magnetic field-dependent SCRP separation fractions β_0 and β_{sat} were fit separately for *E. coli* and in vitro data.

We wrote the rate equations for this model and determined the rate constants from our data. The key steps are outlined below, the details are in the Supporting Information. Our measurements did not directly probe the SCRP dynamics, so we captured the MFE via the magnetic field-dependent separation fraction β(B) and recombination fraction, 1-β(B), from the SCRP states. We used β as a fitting parameter.

We first fit the rates of fluorescence recovery under dim yellow light, k_{recovery}, in the FMN titration data (Figure 6B). From this, we calculated the bimolecular rate constant, k_{ox}, of mSc$^{\cdot-}$ reoxidation by FMN (Figure 6C). We then fit the rates of initial fluorescence quenching, k_{quench}, in the $FMNH_2$ titration data (Figure 6D). By combining k_{ISC}, determined above, with the dependence of k_{quench} on [$FMNH_2$], we determined (1) the bimolecular rate constant k_{red}, for ^{3}mSc reduction by $FMNH_2$ (Figure 6E), and (2) the SCRP separation fraction at zero magnetic field, $\beta_0 \equiv \beta(B = 0)$. We determined $\beta_{\text{sat}} \equiv \beta(B_{\text{sat}})$ by fitting the numerical model to our data on $\Delta F/F_{\text{ss}}$ and $\Delta F/F_{t=0}$ as a function of [FMN] and [$FMNH_2$] (i.e., Figure 4G,H). The best-fit values were β_0 = 0.81 and β_{sat}= 0.93. The fit parameters are given in Table 1 and the model is available as Supplementary Code.

Our model explained many features of our data, both in *E. coli* and with purified protein. In *E. coli*, upon onset of illumination at $I\sigma$ = 11,400 s^{-1}, the mScarlet3 fluorescence initially dropped by more than 100-fold, from 13,000 to 80 counts. Our model reproduced the near-independence of MFE amplitude ($\Delta F/F_{\text{ss}}$) on illumination intensity under conditions of strong quenching (Figure 6F, compare to Figure 1E), the linear dependence of magnetic field-induced switching rate (k_{switch}) on illumination intensity (Figure 6G, compare to Figure 1G), and the independence of k_{switch} on magnetic field strength (acting through $\beta(B)$, Figure S6, compare to Figure 1H).

Table 1. Fit Parameters for the Kinetic Model of the Photocycle

parameter	value	description	source
σ	3.5×10^{-16} cm^2	mScarlet3 absorption cross section at 561 nm	ref 11
k_R^S	2.5×10^8 s^{-1}	inverse of the mScarlet3 excited-state lifetime	ref 11
k_{ISC}	1.85×10^5 s^{-1}	mScarlet3 intersystem crossing rate	fit from Figure 5E
k_R^T	224 s^{-1}	inverse of the mScarlet3 triplet lifetime	fit from Figure 5D
k_{ox}	3375 M^{-1} s^{-1}	oxidation of mScarlet3 radical anion by FMN	fit from Figure 6C
β_0	0.81		fit to numerical model
β_{sat}	0.93	*in vitro*SCRP separation fraction at magnetic field $B = B_{sat}$	fit to numerical model
k_{red}	5×10^7 M^{-1} s^{-1}	reduction of triplet mScarlet3 by $FMNH_2$	fit from Figure 6E
k_{dis}	5×10^9 M^{-1} s^{-1}	rate constant for $FMNH^{\cdot}$ disproportionation	ref 15

Using the parameters determined from our experiments in purified proteins, the maximal predicted MFE in vitro was 14% across all illumination intensities and concentrations of FMN and $FMNH_2$. To match the larger MFE (21%) observed in *E. coli*, we decreased the values of β to $\beta_0 = 0.62$ and $\beta_{sat} = 0.82$. These decreases in β can be attributed to a greater bias toward recombination vs separation in *E. coli* compared to in vitro (Supporting Information). This modification is plausible, considering the influence of nanoscale confinement and crowding in the *E. coli* cytoplasm.

For the experiments with purified protein, the model reproduced the dependence of quenching amplitude ($F_{ss}/F_{t=0}$) on FMN and $FMNH_2$ concentrations (Figure S7). We then simulated the complete experiment of Figure 4F,G, including the initial quenching, the magnetic field-dependent changes in fluorescence, and the recovery of fluorescence under dim yellow light. By varying the nominal flavin concentrations by <30% (to account for possible background redox processes) we achieved close overlay of the predicted and measured traces (Figure 6H,I).

Implications of the Model. We used the kinetic model to explore how to maximize the MFE magnetic field sensitivity and kinetics. The most easily controlled parameters are [FMN], [$FMNH_2$], and light intensity ($I\sigma$). Surprisingly, we found that when the MFE was small, variation in all three parameters caused the absolute MFE, $\Delta F/F_{t=0}$, to vary along a single universal curve parametrized by $x \equiv F_{ss}/F_{t=0}$ i.e., the steady-state residual fluorescence. Specifically, in the limit of small $\Delta\beta \equiv \beta(B) - \beta(0)$, the kinetic equations predicted:

$$\Delta F/F_{t=0} \approx \frac{\Delta\beta}{\beta_0} x(1 - x) \tag{1}$$

$$\Delta F/F_{ss} \approx \frac{\Delta\beta}{\beta_0}(1 - x) \tag{2}$$

(here we have preserved the sign convention $\Delta F \equiv F(0) - F(B)$). The derivation is in the Supporting Information. Eq 1 confirms our earlier observation that the absolute MFE was maximized around $x = 1/2$. In vitro data with variable [FMN], [$FMNH_2$] (Figure 4G,H) and $I\sigma$ (Figure S8) all fell close to eq 1, confirming its universality (Figure 7A). Eq 2 predicts that the relative MFE is largest when the fluorescence is most strongly quenched ($x \approx 0$). In our experiments in *E. coli*, the steady-state residual fluorescence ranged from $x = 2.6\%$ at $I = 0.3$ to $x = 0.6\%$ at $I = 21$ W/cm^2, explaining why we did not detect the intensity-dependent change in $\Delta F/F_{ss}$. This analysis presumes that there is no fluorescent background. Presence of a small fluorescent background shifts the maximal value of $\Delta F/F_{ss}$ to higher x, while having little effect on the maximal value of $\Delta F/F_{t=0}$.

The different conditions for maximizing absolute vs relative MFE highlight a general fact: different chemical quantities may have their magnetic field sensitivity maximized under different conditions. We used the model to predict the time-courses of both observed and unobserved quantities (Figure S9). Figures 7B−F show the dependence on [FMN] and [$FMNH_2$] of $F_{ss}/F_{t=0}$, $\Delta F/F_{ss}$, $\Delta F/F_{t=0}$, the fractional change in mScarlet3$^{\cdot-}$ ($-\Delta mSc^{\cdot-}/mSc^{\cdot-}{}_{ss}$), and the magnetic field-induced switching rate, k_{switch}. Figures S10 and S11 show the dependence of the same variables on the excitation rate, $I\sigma$, and either [FMN] or [$FMNH_2$].

One may wish to use the MFE to detect time-dependent magnetic fields. The switching rate, k_{switch}, is the sum of the rates into and out of the $mSc^{\cdot-}$ state. Under continuous low-intensity illumination, k_{switch} depends linearly on $I\sigma$ and [FMN]. Increasing [$FMNH_2$] increases k_{switch} up until [$FMNH_2$] ≈ 5.5 μM. At high light intensity ($I > 10^6$ W/cm^2), the MFE switching follows a multiexponential, with components corresponding to k_{ISC} and $k_{red} \times$ [$FMNH_2$]. The highest switching rate in our simulations was 1.16×10^5 s^{-1} (Figure S12), though our model might fail at such high light intensities, where other photoreactions could come into play.

An alternate approach to measuring fast (and periodic) magnetic field dynamics is to pulse the illumination in synchrony with the oscillations in magnetic field, and to measure the rate of accumulation of $mSc^{\cdot-}$, i.e. as a light-gated integrator. In this case, one should set [FMN] = 0 so that the $mSc^{\cdot-}$ is long-lived. The time-resolution is set simply by the rate of reaction between ^{3}mSc and $FMNH_2$ to form the SCRP, presuming that the subsequent dynamics are fast. At close-to-saturating [$FMNH_2$] = 1.4 mM,[21,22] this rate is predicted to be 7×10^4 s^{-1}, implying the ability to use this "lock-in" scheme to detect magnetic fields at up to tens of kHz. The maximum concentration of $FMNH_2$ might be increased via addition of hydrotropic agents such as nicotinamide,[23,24] though it is not known how well our model will work at concentrations well outside the range used to determine its parameters.

Modeling the SCRP Dynamics. Our kinetic model places no constraints on the SCRP separation fraction, $\beta(B)$, but in reality this function is governed by the SCRP spin dynamics and reaction kinetics. The SCRP dynamics can be described at varying levels of theory. The Haberkorn master equation provides a fully quantum description,[25] while the rate-based description of Hayashi and Nagakura provides a useful approximation.[26] The model of Hayashi and Nagakura captures the fact that in strong magnetic field, the $T_\pm$ sublevels and the T_0 sublevel are not chemically equivalent: $T_\pm$ are energetically forbidden from interconverting with the singlet state, S, while T_0 and S continue to interconvert in the presence of a strong field.[26] This model predicts that in the limit of fast hyperfine-mediated intersystem crossing, $\beta_0 = 1/\left(1 + \frac{\eta}{2}\right)$, where $\eta \equiv k_{rec}/k_{sep}$ is the ratio of

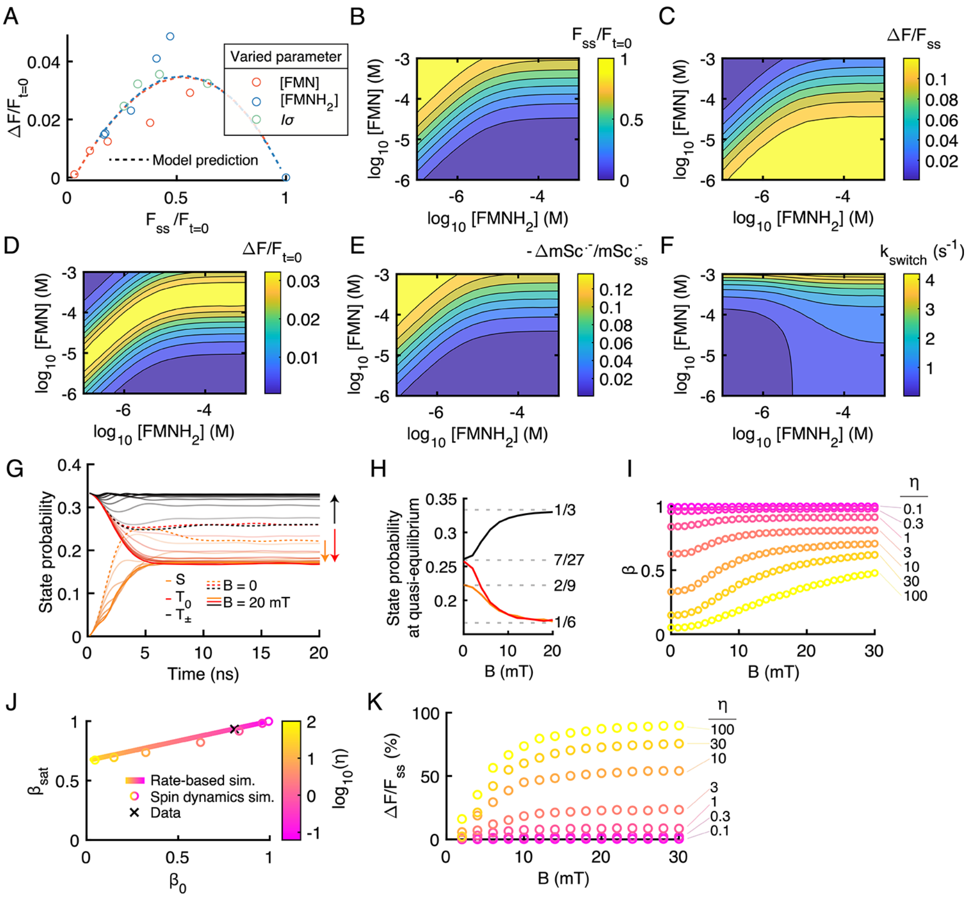

Figure 7. Model predictions for the MFE. (A) Universal curve predicts relation between absolute MFE, $\Delta F/F_{t=0}$, and residual steady-state fluorescence, $x = F_{ss}/F_{t=0}$, when the MFE is small. Variation in [FMN], [$FMNH_2$] and light intensity all led to variations in MFE along this curve. (B−F) Predicted effects of [$FMNH_2$] and [FMN] on (B) $F_{ss}/F_{t=0}$, (C) $\Delta F/F_{ss}$, (D) $\Delta F/F_{t=0}$, (E) ($-\Delta mSc^{-}/mSc^{-}_{ss}$), and (F) k_{switch} for the MFE upstroke. Illumination intensity was assumed to be $I\sigma = 1652\ s^{-1}$, corresponding to 1.7 W/cm^2 at 561 nm. (G) Simulated ensemble-averaged spin-state probabilities for SCRPs initially equally populated in the T_0, T_+, and T_- states. The hyperfine field was Gaussian distributed in three dimensions, with standard deviation 2 mT for each electron spin, and the external magnetic field was varied from 0 − 20 mT. Arrows point from low to high external magnetic field. (H) Magnetic field-dependent spin state probabilities at steady state (20 ns on panel (G)). Probabilities for zero and saturating magnetic fields agree with analytical results. (I) Simulated SCRP separation fraction, β, as a function of magnetic field strength, at varying values of $\eta = k_{rec}/k_{sep}$. (J) Relation between values of β under saturating-field vs zero-field, for different values of η. The rate-based simulation (solid line) has intercept 2/3 and slope 1/3. Semiclassical spin dynamics simulation (circles) and experimental result (x) lie near this line. (K) Predicted MFE amplitude as a function of magnetic field for varying values of η. In these simulations, we kept constant [FMN] = 0.38 μM, [$FMNH_2$] = 6 μM.

recombination and separation rate constants. The model further predicts that $\beta_{sat} = 2/3 + 1/3\beta_0$ (Figure 7J). This simple result is a strong constraint on the maximal MFE amplitude. Remarkably, the values of β we determined by fitting the kinetic photocycle model to our in vitro data, β_0 = 0.81 and β_{sat} = 0.93, lie within 1% of this line (i.e., 2/3 + 1/3 × 0.81 = 0.94), establishing good concordance of model and experiment.

The Hayashi and Nagakura model has two limitations: (1) as a rate-based model it may miss effects due to the coherent electron spin dynamics; and (2) it only predicts the limiting dynamics in zero and saturating magnetic fields, not the intermediate cases. To address these limitations, we calculated $\beta(B)$ by simulating the quantum dynamics and reaction kinetics of the SCRP spins (Supporting Information). Briefly, SCRP spins were initialized with equal populations in T_0, T_+, and T_- states, and set in motion precessing around local random hyperfine fields plus the external magnetic field. The singlet and triplet probabilities were calculated as a function of time. In the absence of chemical reactions, the ensemble-average state occupancies agreed with prior analytical predictions (Figure 7G,H).[27,28] To introduce chemical reactions, at each time-step we let each SCRP either separate, with a rate constant k_{sep} (assumed to be the same for singlet and triplet states), or recombine, with a rate constant $k_{rec}(1 - \alpha(t))$, where $(1 - \alpha(t))$ is the time-dependent probability of being in the singlet state (Figure S13).

We tallied the fraction of SCRPs that separated to determine $\beta(B)$. We then repeated this process for a range of values of $\eta \equiv k_{rec}/k_{sep}$ (Figure 7I). These semiclassical spin dynamics simulations gave values of β_{sat} and β_0 which were very close to the rate-based result $\beta_{sat} \approx 2/3 + 1/3\beta_0$ (Figure 7J). We then input the simulated $\beta(B)$ values into our model of the photocycle (Figure 6A) to determine the $\Delta F/F_{ss}$ vs B curves for different values of η (Figure 7K). As k_{sep} approached zero (e.g., large η), $\Delta F/F_{ss}$ approached 100%.

■ DISCUSSION

We determined the mechanism by which small magnetic fields can modulate the fluorescence of mScarlet3. The reaction requires the simultaneous presence of fully reduced $FMNH_2$ and oxidized FMN, and involves a photocycle comprising reduction of triplet-state mScarlet3 by $FMNH_2$, and reoxidation of $mScarlet3^{\cdot-}$ by FMN. A numerical model quantitatively reproduced the time-dependent fluorescence trajectories under varied conditions of FMN, $FMNH_2$, illumination intensity, and magnetic field, both in vitro and in live *E. coli*. We infer that live *E. coli* cytoplasm contains sufficient FMN and $FMNH_2$ (or perhaps other oxidant and reductant), so the MFE does not require blue light. Previous work has shown that other redox cofactors such as cinnavalininate and WST-8 can also enable the MFE.[1]

Some molecular details in our model remain uncertain. The molecular structure of the putative $mScarlet3^{\cdot-}$ is not known. Many red fluorescent proteins—KillerRed, mRFP, DsRed, and mKate2—accept electrons upon photoexcitation,[29−31] suggesting the presence of a common mechanism. Electron spin resonance (ESR) studies may provide insights into the nature of the radical anion. The detailed mechanism underlying electron-transfer between $FMNH_2$ and ^{3}mSc is also unknown. Fluorescent proteins undergo multiple light-driven redox reactions, some involving direct electron-transfer between the chromophore and an external redox species, and some involving hopping mediated by other amino acids in the protein.[31] Further mutagenesis, transient absorption, and computational studies will be needed to elucidate the details of this reaction step.

In organic donor−acceptor complexes, the MFE can be enhanced by tethering the groups together,[5,32] or by confinement in micelles.[10,33] In the context of our model, these effects can be understood as decreasing the rate of SCRP separation (i.e., increasing η), which would decrease β_0 and β_{sat} and would increase $\beta_{sat} - \beta_0$. Thus, tethering the flavin cofactor or nanoconfinement (in micelles, vesicles, or pores in a gel) may substantially enhance the MFE amplitude. Tethering a fluorescent protein to a flavin-binding domain may enable development of magneto-switchable proteins in mammalian cells, a necessary step for opaque-tissue applications of magnetogenetics.

To increase the magnetic field sensitivity, one could decrease the strength of the hyperfine coupling at the locations of the spins. It may be possible to identify redox cofactors that have weaker hyperfine couplings than $FMNH^{\cdot}$, e.g., by replacing the H with deuterium at position N5 in FMN.[34] Whether directed evolution can modulate the hyperfine environment for the electron spin on $mSc^{\cdot-}$ remains an open question.

CONCLUSIONS

A detailed mechanistic understanding of spin states in fluorescent proteins may lead to new microscopy and sensing techniques.[35,36] For example, a recent study demonstrated fluorescence-detected electron-spin resonance via optical pumping of the triplet state in yellow fluorescent protein (YFP).[37] Other recent studies showed fluorescence-detected electron-spin resonance in a modified LOV domain, magLOV,[38] in mScarlet in a live nematode,[39] and in a cryptochrome.[40] In organic solutions showing magnetic-sensitive fluorescence, imaging through a scattering medium was achieved by sweeping a magnetic null through the sample.[41] Development of protein-based spintronics requires a detailed understanding of both the quantum spin dynamics and the kinetics of the photocycles in which these spin dynamics are embedded.

Photoredox reactions are common in proteins: cryptochromes and photolyases contain flavin cofactors,[42] and protein backbones can donate electrons to photoexcited FMN.[7,42] Among fluorescent proteins, GFP can donate an electron from the excited state, undergoing oxidative redding.[43,44] Under anaerobic conditions, GFP may also accept an electron.[44−46] We suspect that many proteins with these properties may be magnetic field-sensitive or could be engineered to show magnetosensitivity under suitable conditions.

It remains controversial whether radical pair-based magnetic field effects have any biological function.[47,48] The half-maximal field of 5.5 mT in our experiments is approximately 100-fold larger than Earth's magnetic field, so our experiments do not directly address this controversy. Regardless, the existence of strong MFEs in proteins under physiological conditions suggests that such effects may be more widespread than currently appreciated. An exciting future opportunity is to use the power of protein design and directed evolution to tune the MFE amplitude, magnetic field sensitivity, and switching kinetics; and to couple the MFE to downstream biochemical cascades.

ASSOCIATED CONTENT

Supporting Information

The Supporting Information is available free of charge at https://pubs.acs.org/doi/10.1021/jacs.5c03997.

> Experimental details, materials, and methods; characterization of the MFE, control experiments, and additional simulation predictions; mathematical modeling and fitting of the MFE and spin dynamics simulations; and code for the photocycle kinetic model and SCRP spin dynamics simulations is available at https://github.com/adamcohenlab/xiang2025mfe (PDF)

AUTHOR INFORMATION

Corresponding Author

Adam E. Cohen − *Department of Physics and Department of Chemistry and Chemical Biology, Harvard University, Cambridge, Massachusetts 02138, United States;* orcid.org/0000-0002-8699-2404; Email: cohen@chemistry.harvard.edu

Authors

Katherine M. Xiang − *Department of Physics, Harvard University, Cambridge, Massachusetts 02138, United States*

Hana Lampson − *Department of Physics, Harvard University, Cambridge, Massachusetts 02138, United States*

Rebecca Frank Hayward − *School of Engineering and Applied Sciences, Harvard University, Cambridge, Massachusetts 02138, United States*

Andrew G. York − *Calico Life Sciences LLC, South San Francisco, California 94080, United States*

Maria Ingaramo − *Calico Life Sciences LLC, South San Francisco, California 94080, United States*

Complete contact information is available at: https://pubs.acs.org/10.1021/jacs.5c03997

Notes

The authors declare no competing financial interest.

■ ACKNOWLEDGMENTS

We thank Madeleine Howell, Felix Sigmund, Daniel G. Itkis, Xiang Wu, F. Phil Brooks III, Peter Maurer, Uri Zvi, Ben Soloway, and Jacob Feder for helpful discussions and technical assistance. This work was supported by the Gordon and Betty Moore Foundation and NSF Quantum Sensing for Biophysics and Bioengineering (QuBBE) Quantum Leap Challenge Institute (QLCI) grant OMA-2121044. K.M.X. was supported by a Hertz Foundation Fellowship and an NSF Graduate Research Fellowship DGE 2140743.

■ REFERENCES

(1) Hayward, R. F.; Lazzari-Dean, J. R.; York, A. G.; Ingaramo, M.Magnetic Control of GFP-like Fluorescent Proteins. In *Proc. SPIE PC12863, Quantum Effects and Measurement Techniques in Biology and Biophotonics*; SPIE, 2023.

(2) Turro, N. J.; Kraeutler, B. Magnetic Field and Magnetic Isotope Effects in Organic Photochemical Reactions. A Novel Probe of Reaction Mechanisms and a Method for Enrichment of Magnetic Isotopes. *Acc. Chem. Res.* **1980**, *13* (10), 369−377.

(3) Turro, N. J.; Kraeutler, B. Magnetic Isotope and Magnetic Field Effects on Chemical Reactions. Sunlight and Soap for the Efficient Separation of Carbon-13 and Carbon-12. *J. Am. Chem. Soc.* **1978**, *100* (23), 7432−7434.

(4) Cao, H.; Fujiwara, Y.; Haino, T.; Fukazawa, Y.; Tung, C. H.; Tanimoto, Y. Magnetic Field Effects on Intramolecular Exciplex Fluorescence of Chain-Linked Phenanthrene and N, N-Dimethylaniline: Influence of Chain Length, Solvent, and Temperature. *Bull. Chem. Soc. Jpn.* **1996**, *69* (10), 2801−2813.

(5) Lee, H.; Yang, N.; Cohen, A. E. Mapping Nanomagnetic Fields Using a Radical Pair Reaction. *Nano Lett.* **2011**, *11*, 5367−5372.

(6) Ikeya, N.; Woodward, J. R. Cellular Autofluorescence Is Magnetic Field Sensitive. *Proc. Natl. Acad. Sci. U.S.A.* **2021**, *118* (3), No. e2018043118.

(7) Kattnig, D. R.; Evans, E. W.; Déjean, V.; Dodson, C. A.; Wallace, M. I.; Mackenzie, S. R.; Timmel, C. R.; Hore, P. J. Chemical Amplification of Magnetic Field Effects Relevant to Avian Magnetoreception. *Nature Chem.* **2016**, *8* (4), 384−391.

(8) Xu, J.; Jarocha, L. E.; Zollitsch, T.; Konowalczyk, M.; Henbest, K. B.; Richert, S.; Golesworthy, M. J.; Schmidt, J.; Déjean, V.; Sowood, D. J. C.; Bassetto, M.; Luo, J.; Walton, J. R.; Fleming, J.; Wei, Y.; Pitcher, T. L.; Moise, G.; Herrmann, M.; Yin, H.; Wu, H.; Bartölke, R.; Käsehagen, S. J.; Horst, S.; Dautaj, G.; Murton, P. D. F.; Gehrckens, A. S.; Chelliah, Y.; Takahashi, J. S.; Koch, K.-W.; Weber, S.; Solov'yov, I. A.; Xie, C.; Mackenzie, S. R.; Timmel, C. R.; Mouritsen, H.; Hore, P. J. Magnetic Sensitivity of Cryptochrome 4 from a Migratory Songbird. *Nature* **2021**, *594* (7864), 535−540.

(9) Takiff, L.; Boxer, S. G. Phosphorescence from the Primary Electron Donor in Rhodobacter Sphaeroides and Rhodopseudomonas Viridis Reaction Centers. *Biochimica et Biophysica Acta (BBA) - Bioenergetics* **1988**, *932*, 325−334.

(10) Steiner, U. E.; Ulrich, T. Magnetic Field Effects in Chemical Kinetics and Related Phenomena. *Chem. Rev.* **1989**, *89* (1), 51−147.

(11) Gadella, T. W. J.; Van Weeren, L.; Stouthamer, J.; Hink, M. A.; Wolters, A. H. G.; Giepmans, B. N. G.; Aumonier, S.; Dupuy, J.; Royant, A. mScarlet3: A Brilliant and Fast-Maturing Red Fluorescent Protein. *Nat. Methods* **2023**, *20* (4), 541−545.

(12) Holmström, B.; Oster, G. Riboflavin as an Electron Donor in Photochemical Reactions. *J. Am. Chem. Soc.* **1961**, *83* (8), 1867−1871.

(13) Song, S.-H.; Dick, B.; Penzkofer, A. Photo-Induced Reduction of Flavin Mononucleotide in Aqueous Solutions. *Chem. Phys.* **2007**, *332* (1), 55−65.

(14) Penzer, G. R. The Chemistry of Flavins and Flavoproteins: Aerobic Photochemistry. *Biochem. J.* **1970**, *116* (4), 733−743.

(15) Holmström, B. Flash Photoreduction of Flavin Mono Nucleotide in Neutral Solutions: Absolute Absorptivity of the Semiquinone. *Photochem. & Photobiology* **1964**, *3* (2), 97−114.

(16) Vaish, S. P.; Tollin, G. Flash Photolysis of Flavins. V. Oxidation and Disproportionation of Flavin Radicals. *J. Bioenerg Biomembr* **1971**, *2* (2), 61−72.

(17) Holzer, W.; Shirdel, J.; Zirak, P.; Penzkofer, A.; Hegemann, P.; Deutzmann, R.; Hochmuth, E. Photo-Induced Degradation of Some Flavins in Aqueous Solution. *Chem. Phys.* **2005**, *308* (1−2), 69−78.

(18) Heelis, P. F.; Parsons, B. J.; Phillips, G. O.; McKellar, J. F. The photoreduction of flavins by amino acids and EDTA. A continuous and flash photolysis study. *Photochem. & Photobiology* **1979**, *30* (3), 343−347.

(19) Draper, R. D.; Ingraham, L. L. A Potentiometric Study of the Flavin Semiquinone Equilibrium. *Arch. Biochem. Biophys.* **1968**, *125* (3), 802−808.

(20) Berg, H. C. *Random Walks in Biology*; Princeton University Press: Princeton, NJ, 1993.

(21) Guo, A. C.; Jewison, T.; Wilson, M.; Liu, Y.; Knox, C.; Djoumbou, Y.; Lo, P.; Mandal, R.; Krishnamurthy, R.; Wishart, D. S. ECMDB: The E. Coli Metabolome Database. *Nucleic Acids Res.* **2012**, *41* (D1), D625−D630.

(22) Sajed, T.; Marcu, A.; Ramirez, M.; Pon, A.; Guo, A. C.; Knox, C.; Wilson, M.; Grant, J. R.; Djoumbou, Y.; Wishart, D. S. ECMDB 2.0: A Richer Resource for Understanding the Biochemistry of *E. Coli*. *Nucleic Acids Res.* **2016**, *44* (D1), D495−D501.

(23) Coffman, R. E.; Kildsig, D. O. Effect of Nicotinamide and Urea on the Solubility of Riboflavin in Various Solvents. *J. Pharm. Sci.* **1996**, *85* (9), 951−954.

(24) Orita, A.; Verde, M. G.; Sakai, M.; Meng, Y. S. A Biomimetic Redox Flow Battery Based on Flavin Mononucleotide. *Nat. Commun.* **2016**, *7* (1), 13230.

(25) Haberkorn, R. Density Matrix Description of Spin-Selective Radical Pair Reactions. *Mol. Phys.* **1976**, *32* (5), 1491−1493.

(26) Hayashi, H.; Nagakura, S. Theoretical Study of Relaxation Mechanism in Magnetic Field Effects on Chemical Reactions. *Bull. Chem. Soc. Jpn.* **1984**, *57* (2), 322−328.

(27) Schulten, K.; Wolynes, P. G. Semiclassical Description of Electron Spin Motion in Radicals Including the Effect of Electron Hopping. *J. Chem. Phys.* **1978**, *68* (7), 3292−3297.

(28) Cohen, A. E. Nanomagnetic Control of Intersystem Crossing. *J. Phys. Chem. A* **2009**, *113* (41), 11084−11092.

(29) Vegh, R. B.; Bravaya, K. B.; Bloch, D. A.; Bommarius, A. S.; Tolbert, L. M.; Verkhovsky, M.; Krylov, A. I.; Solntsev, K. M. Chromophore Photoreduction in Red Fluorescent Proteins Is Responsible for Bleaching and Phototoxicity. *J. Phys. Chem. B* **2014**, *118* (17), 4527−4534.

(30) Protasova, E. A.; Mishin, A. S.; Lukyanov, K. A.; Maksimov, E. G.; Bogdanov, A. M. Chromophore Reduction plus Reversible Photobleaching: How the mKate2 "Photoconversion" Works. *Photochem. Photobiol. Sci.* **2021**, *20* (6), 791−803.

(31) Acharya, A.; Bogdanov, A. M.; Grigorenko, B. L.; Bravaya, K. B.; Nemukhin, A. V.; Lukyanov, K. A.; Krylov, A. I. Photoinduced Chemistry in Fluorescent Proteins: Curse or Blessing? *Chem. Rev.* **2017**, *117* (2), 758−795.

(32) Lee, H.; Brinks, D.; Cohen, A. E. Two-Photon Imaging of a Magneto-Fluorescent Indicator for 3D Optical Magnetometry. *Opt. Express, OE* **2015**, *23* (21), 28022−28030.

(33) Ulrich, T.; Steiner, U. E. Magnetic-Field-Dependent Recombination Kinetics of Geminate Radical Pairs in Reversed Micelles of Variable Size. *Chem. Phys. Lett.* **1984**, *112* (4), 365−370.

(34) Rostas, A.; Einholz, C.; Illarionov, B.; Heidinger, L.; Said, T. A.; Bauss, A.; Fischer, M.; Bacher, A.; Weber, S.; Schleicher, E. Long-Lived Hydrated FMN Radicals: EPR Characterization and Implications for Catalytic Variability in Flavoproteins. *J. Am. Chem. Soc.* **2018**, *140* (48), 16521−16527.

(35) Byrdin, M.; Duan, C.; Bourgeois, D.; Brettel, K. A Long-Lived Triplet State Is the Entrance Gateway to Oxidative Photochemistry in

Green Fluorescent Proteins. *J. Am. Chem. Soc.* **2018**, *140* (8), 2897−2905.

(36) Ludvikova, L.; Simon, E.; Deygas, M.; Panier, T.; Plamont, M.-A.; Ollion, J.; Tebo, A.; Piel, M.; Jullien, L.; Robert, L.; Le Saux, T.; Espagne, A. Near-Infrared Co-Illumination of Fluorescent Proteins Reduces Photobleaching and Phototoxicity. *Nat. Biotechnol.* **2024**, *42* (6), 872−876.

(37) Feder, J. S.; Soloway, B. S.; Verma, S.; Geng, Z. Z.; Wang, S.; Kifle, B.; Riendeau, E. G.; Tsaturyan, Y.; Weiss, L. R.; Xie, M.; Huang, J.; Esser-Kahn, A.; Gagliardi, L.; Awschalom, D. D.; Maurer, P. C. A Fluorescent-Protein Spin Qubit. arXiv, 2024.

(38) Abrahams, G.; Spreng, V.; Štuhec, A.; Kempf, I.; James, J.; Sechkar, K.; Stacey, S.; Trelles-Fernandez, V.; Antill, L. M.; Ingaramo, M.; York, A.; Tetienne, J.-P.; Timmel, C. R.; Steel, H. Quantum Spin Resonance in Engineered Magneto-Sensitive Fluorescent Proteins Enables Multi-Modal Sensing in Living Cells. bioRxiv, **2024**.

(39) Burd, S. C.; Bagheri, N.; Ingaramo, M.; Condon, A. F.; Mondal, S.; Dowlatshahi, D. P.; Summers, J. A.; Mukherjee, S.; York, A. G.; Wakatsuki, S.; Boxer, S. G.; Kasevich, M. Magnetic Resonance Control of Reaction Yields through Genetically-Encoded Protein:-Flavin Spin-Correlated Radicals in a Live Animal. bioRxiv, 2025.

(40) Meng, K.; Nie, L.; Berger, J.; von Grafenstein, N. R.; Einholz, C.; Rizzato, R.; Schleicher, E.; Bucher, D. B. Optically Detected and Radio Wave-Controlled Spin Chemistry in Cryptochrome. arXiv, 2025.

(41) Yang, N.; Cohen, A. E. Optical Imaging through Scattering Media via Magnetically Modulated Fluorescence. *Opt. Express* **2011**, *19*, 25461.

(42) Evans, E. W.; Dodson, C. A.; Maeda, K.; Biskup, T.; Wedge, C. J.; Timmel, C. R. Magnetic Field Effects in Flavoproteins and Related Systems. *Interface Focus.* **2013**, *3* (5), 20130037.

(43) Bogdanov, A. M.; Mishin, A. S.; Yampolsky, I. V.; Belousov, V. V.; Chudakov, D. M.; Subach, F. V.; Verkhusha, V. V.; Lukyanov, S.; Lukyanov, K. A. Green Fluorescent Proteins Are Light-Induced Electron Donors. *Nat. Chem. Biol.* **2009**, *5* (7), 459−461.

(44) Bogdanov, A. M.; Acharya, A.; Titelmayer, A. V.; Mamontova, A. V.; Bravaya, K. B.; Kolomeisky, A. B.; Lukyanov, K. A.; Krylov, A. I. Turning On and Off Photoinduced Electron Transfer in Fluorescent Proteins by π-Stacking, Halide Binding, and Tyr145 Mutations. *J. Am. Chem. Soc.* **2016**, *138* (14), 4807−4817.

(45) Elowitz, M. B.; Surette, M. G.; Wolf, P.-E.; Stock, J.; Leibler, S. Photoactivation Turns Green Fluorescent Protein Red. *Curr. Biol.* **1997**, *7* (10), 809−812.

(46) Sawin, K. E.; Nurse, P. Photoactivation of Green Fluorescent Protein. *Curr. Biol.* **1997**, *7* (10), R606−R607.

(47) Bassetto, M.; Reichl, T.; Kobylkov, D.; Kattnig, D. R.; Winklhofer, M.; Hore, P. J.; Mouritsen, H. No Evidence for Magnetic Field Effects on the Behaviour of Drosophila. *Nature* **2023**, *620* (7974), 595−599.

(48) Kyriacou, C. P. Magnetic Field Responses in Drosophila. *Nature* **2024**, *629* (8010), E3−E5.

(49) Aumonier, S.; Dupuy, J.; Royant, A. *Structure of the Red Fluorescent Protein mScarlet3 at pH 7.5*; ANR, 2022.

(50) Sehnal, D.; Bittrich, S.; Deshpande, M.; Svobodová, R.; Berka, K.; Bazgier, V.; Velankar, S.; Burley, S. K.; Koča, J.; Rose, A. S. Mol* Viewer: Modern Web App for 3D Visualization and Analysis of Large Biomolecular Structures. *Nucleic Acids Res.* **2021**, *49* (W1), W431−W437.

(51) Berman, H. M. The Protein Data Bank. *Nucleic Acids Res.* **2000**, *28* (1), 235−242.

Supporting Information

Mechanism of giant magnetic field effect in a red fluorescent protein

Katherine M. Xiang[1], Hana Lampson[1], Rebecca Frank Hayward[2], Andrew G. York[4], Maria Ingaramo[4], Adam E. Cohen[1, 3, *]

[1]Department of Physics, Harvard University, Cambridge, MA 02138, USA
[2]School of Engineering and Applied Sciences, Harvard University, Cambridge, MA 02138, USA
[3]Department of Chemistry and Chemical Biology, Harvard University, Cambridge, MA 02138, USA
[4]Calico Life Sciences LLC, South San Francisco, CA 94080, USA

Table of Contents

Experimental Section

Bacterial culture and sample preparation

6xHis-tagged pDx_mScarlet3 (Addgene #189754) was expressed in BL21 (DE3) *E. coli* (NEB C2527H) and plated on lysogeny broth (LB) agar plates with 100 µg/mL Kanamycin (Teknova L1025). The plasmid sequence was verified through whole-plasmid sequencing (Plasmidsaurus). Bacteria were grown at 37 °C overnight. The next day, a single colony was inoculated in 5 mL of LB supplemented with 50 µg/mL Kanamycin and grown in a shaking incubator at 37 °C and 250 r.p.m. overnight.

250 µL from the liquid culture was used to inoculate a 25 mL culture. After 1 hour in a shaking incubator at 37 °C, L-Rhamnose (Promega L5701) was added to a final concentration of 0.2% (w/v) to induce mScarlet3 expression. Bacteria were grown for 4 additional hours to an OD700 of ~0.4. The culture was stored overnight at 4 °C. The liquid culture was imaged the next day.

The culture medium was aspirated and 2 µL of the wet pellet was mounted between a glass slide and a #1.5 coverslip and sealed with clear nail polish.

For the initial screening for MFEs (Fig. S1), samples were grown uninduced on LB agar plates with the appropriate selection antibiotic. The additional fluorescent proteins tested were mScarlet-I3 (Addgene #189757), mRuby3 (Addgene #104005), mSandy2 (Addgene #177760), and mKate2 (Addgene #104030).

Protein purification

His-tagged mScarlet3 was purified using Ni-NTA affinity columns and the kit protocol and buffers (Qiagen 30600). A 10 mL overnight culture was used to inoculate a 250 mL culture. After 1 hour in a shaking incubator at 37 °C, L-Rhamnose (Promega L5701) was added to a final concentration of 0.2% (w/v) to induce mScarlet3 expression. Bacteria were grown for 4 additional hours, and then stored overnight at 4 °C. Cells were harvested by centrifugation at 3400 g for 20 minutes and frozen at -20 °C overnight. The pellet was thawed for 15 minutes on ice and resuspended in 10 mL native Lysis Buffer with one tablet of cOmplete™ Protease Inhibitor Cocktail (Roche 11836170001). The cell lysate was centrifuged at 14,000 g for 30 minutes at 4 °C, and the supernatant was applied to the Fast Start Column. The column was washed twice with 4 mL of Native Wash Buffer. The protein was eluted in two 1 mL fractions of Native Elution Buffer. Imidazole was removed via by spin column filtration. Samples were measured in 1x PBS buffer. Concentrations were quantified using a Nanodrop, using ε_{570} = 104,000 M^{-1} cm^{-1}. For immobilized mScarlet3 experiments, agar Ni-NTA beads from the purification resin were washed with PBS and imaged.

Fluorescence measurements

Samples were imaged on a home-built inverted epifluorescence microscope with 488 nm, 532 nm, and 561 nm laser lines. The beams were combined using dichroic mirrors and sent through an acousto-optic tunable filter (AOTF; Gooch and Housego TF525-250-6-3-GH18A) for temporal modulation of intensity of each wavelength. The beams were expanded and focused to the backfocal plane of an objective (Olympus 20X/1.00 W XLUMPLANFL, or Olympus 40x/0.85 UPlanApo) installed in an Olympus IX71 microscope. None of the elements of the sample stage was magnetic.

Excitation light was separated from fluorescence emission with a 562 nm edge dichroic mirror (Semrock Di02-FF562) and a 575 nm long-pass emission filter (Chroma ET575lp). In experiments where FMN fluorescence was monitored, a quad-edge dichroic (Semrock Di01-405/488/561/635) was used with a dual band emission filter (Chroma ZET488/561m). Emission light was sent to an imaging spectrometer (Horiba iHR320) equipped with an EMCCD camera (Andor iXon EM+). For imaging experiments, the zeroth order was taken from the spectrometer and the slit was set to the maximum width of 60 mm, allowing the full image to pass through to the camera. For measurements of fluorescence emission spectra, we calibrated the linear pixel-to-wavelength correspondence by sending the laser lines directly through using a 50/50 beamsplitter. We used a 1–2 mm entrance slit width for measurements on the microscope. Data were five-point moving average filtered.

Data in Fig. 3 were taken using the same excitation lasers. The zeroth order from the AOTF was expanded to illuminate a quartz cuvette (Starna Cells 23-G-5). A mirror on one side of the cuvette were used to achieve two 10 mm passes of the excitation light through the cuvette. The emission was collected perpendicular to the excitation using a fiber and collimated into the same imaging spectrometer with a 2 mm entrance slit width. Excitation lasers were temporally modulated using physical shutters.

Magnetic fields were modulated by using a permanent magnet (K&J Magnetics B666) mounted on a servo motor. The distance from the sample was adjusted to control the field strength. Square wave magnetic fields were applied with a ~200 ms rise time, with field strength and timing measured by a Hall effect sensor (Texas Instruments DRV5055A4QLPG).

The AOTF, shutters, servo, and the camera were synchronized via a National Instruments Data Acquisition System (DAQ) and custom software (https://www.luminosmicroscopy.com/).

All measurements were performed at 22 °C (295 K).

Absorption measurements

Absorption spectra were taken with a path length of 5 mm (Starna Cells 23-G-5) using a UV-VIS-NIR lamp (Mikropack DH-2000). The same fiber was used to collect transmitted light and fluorescence emission. The transmission light filled the volume of the sample. Physical shutters for the transmitted light and for the excitation light were modulated separately. The transmission light used for absorption measurements was dim, to avoid exciting fluorescence or driving photoswitching.

Supplementary Figures

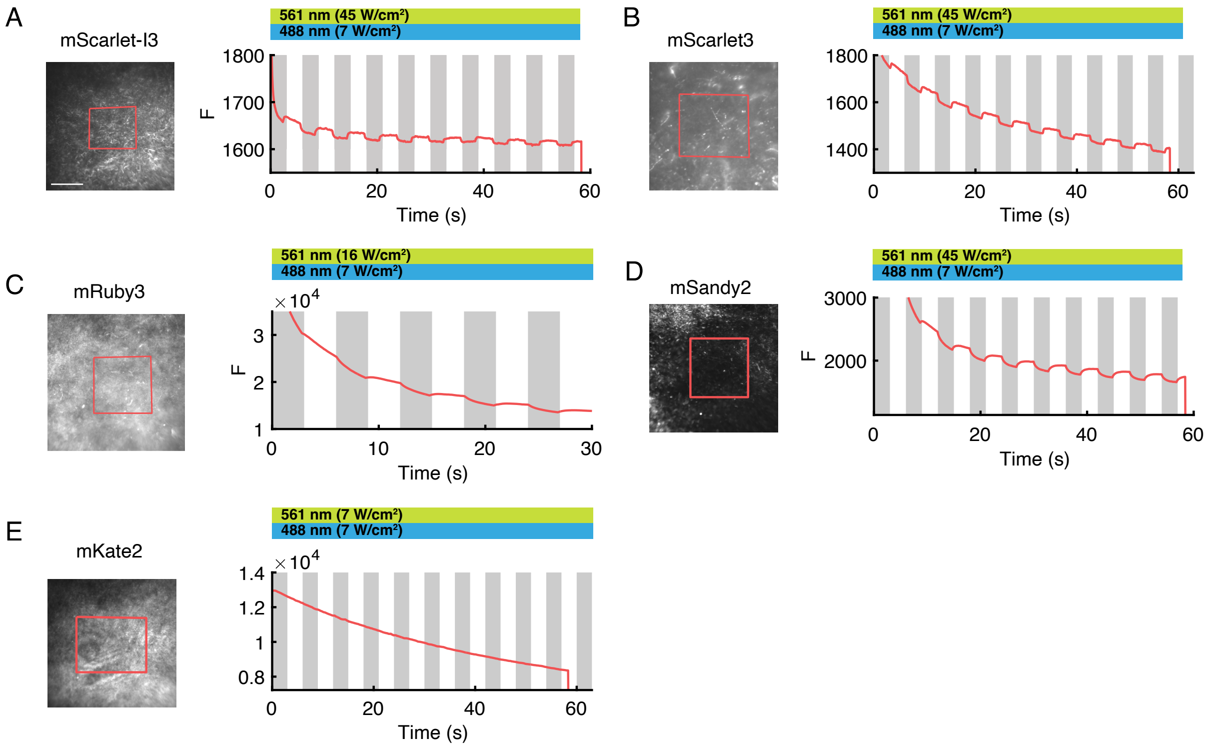

Figure S1. Magnetic field effects in red fluorescent proteins.

E. coli expressing red-emitting fluorescent proteins were grown on LB (lysogeny broth) agar plates and then imaged in an epifluorescence microscope. Panels show responses to a 10 mT magnetic field (grey bars). A 595 nm long-pass emission filter was used. A) mScarlet-I3, B) mScarlet3[1], C) mRuby3[2], D) mSandy2[3], E) mKate2[4].

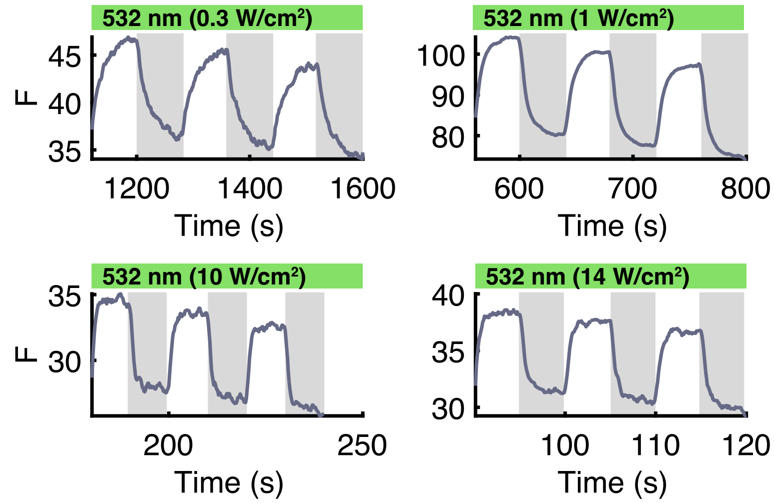

Figure S2. MFE kinetics depend on light intensity.
MFE switching kinetics in *E. coli* at different illumination intensities. Plots show fluorescence after initial fluorescence has quenched to a steady-state.

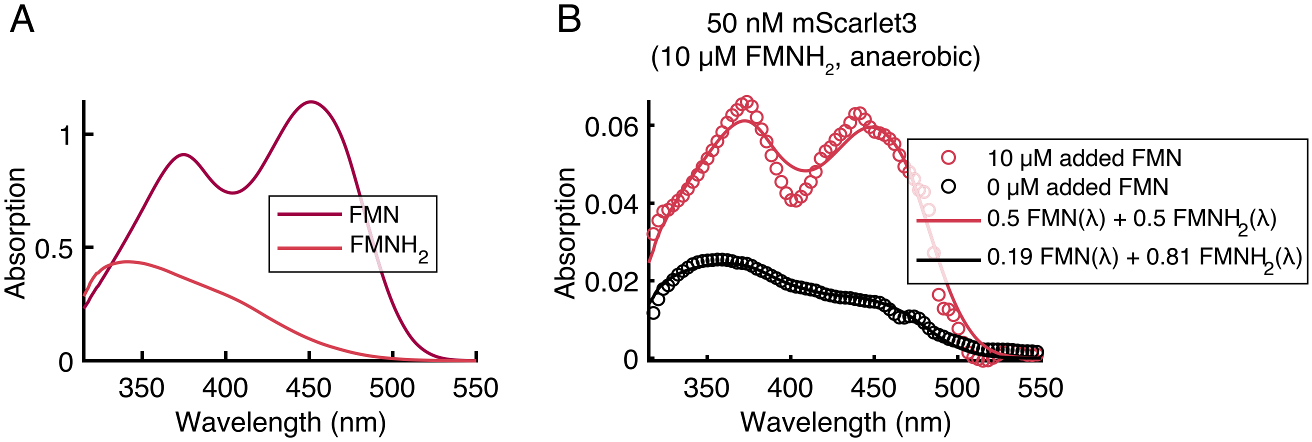

Figure S3. Flavin absorption spectra.
A) Absorption spectra of pure FMN and $FMNH_2$. The spectrum for $FMNH_2$ was measured immediately after photoreduction in the presence of 50 mM EDTA under anaerobic conditions. B) Absorption spectra for the samples in Fig. 4G, comprising 10 μM of photoreduced FMN (nominally $FMNH_2$) and either 10 μM or 0 μM additional FMN. The black curve shows that the nominal 10 μM $FMNH_2$ contained 2 μM FMN, due to incomplete photoreduction.

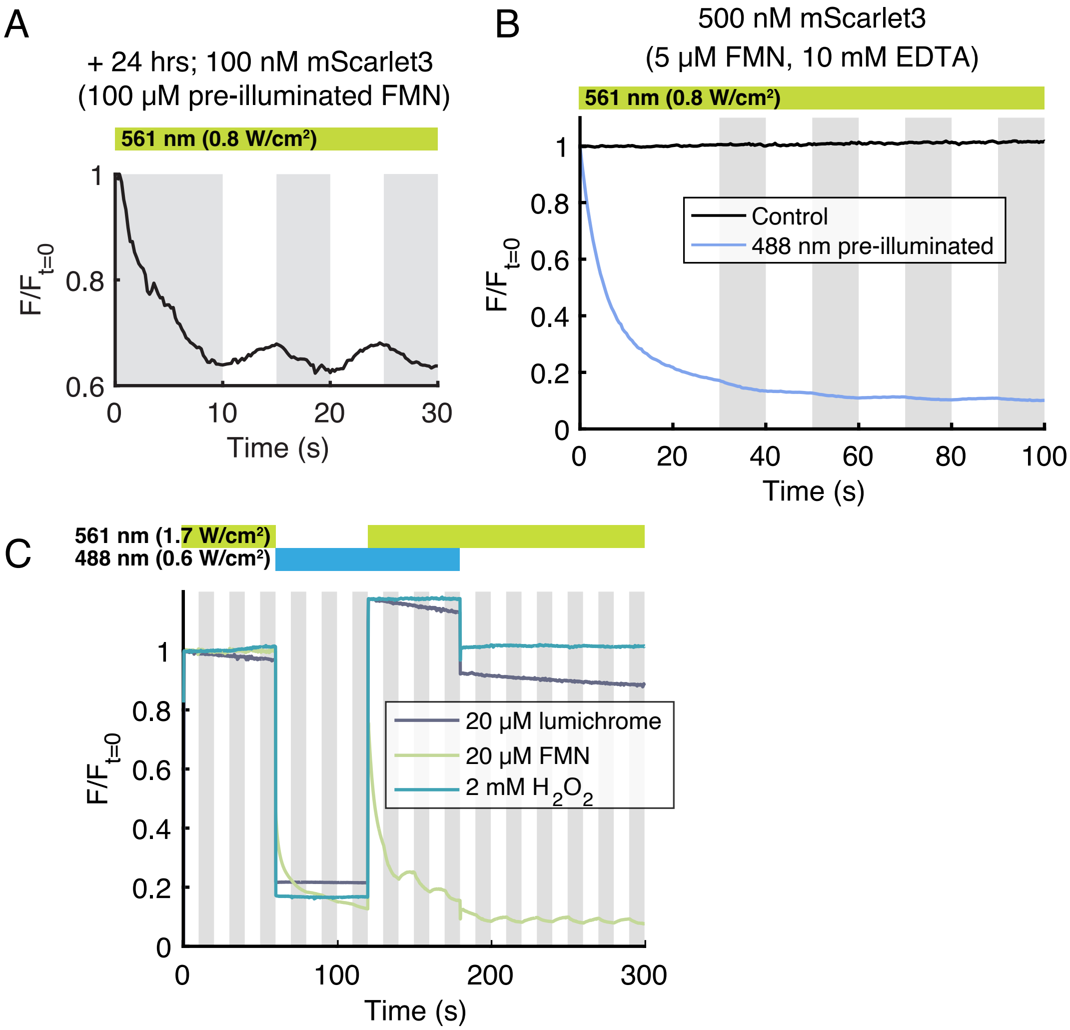

Figure S4. Control experiments ruling out photoproducts other than $FMNH_2$ as the mediator of the MFE.

A) $FMNH_2$ was photochemically produced by illuminating 100 μM FMN with 488 nm light, under anaerobic conditions. The $FMNH_2$ was then combined with mScarlet3 and then stored at room temperature in the dark under anaerobic conditions for 24 h. Under yellow light alone, the sample showed a clear MFE, indicating the stability of the FMN photoproduct under these conditions. B) mScarlet3, FMN, and 10 mM EDTA were combined under anaerobic conditions. The sample showed no quenching or MFE upon 561 nm illumination, indicating that EDTA does not reduce FMN under these conditions. The sample was then pre-illuminated with 488 nm light. Upon onset of yellow illumination, the mScarlet3 fluorescence quenched and showed an MFE, as expected. C) mScarlet3 did not show an MFE when combined with other FMN photoproducts including lumichrome (mScarlet3 at 500 nM) or H_2O_2 (mScarlet3 at 5 μM), under either 488 nm, 561 nm, or combined 488 + 561 nm illumination. Trace with 500 nM mScarlet3 and 20 μM FMN shown for comparison. All samples were measured under anaerobic conditions.

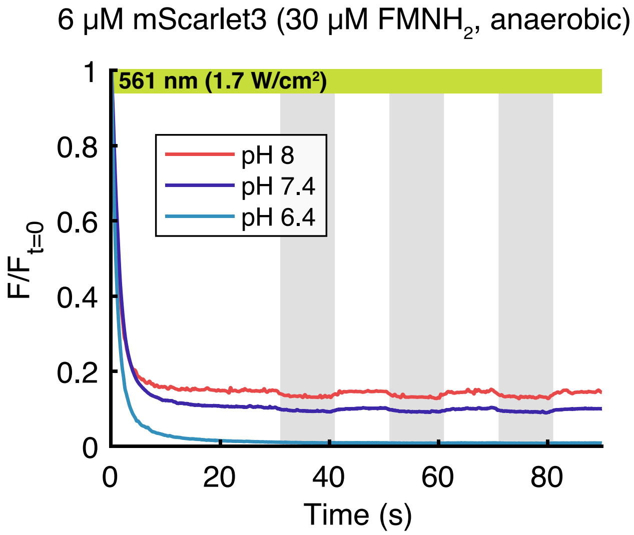

Figure S5. pH dependence of mScarlet3 fluorescence quenching.
The greater quenching at lower pH is consistent with $FMNH_2$ being the reductant, rather than $FMNH^{\bullet-}$.

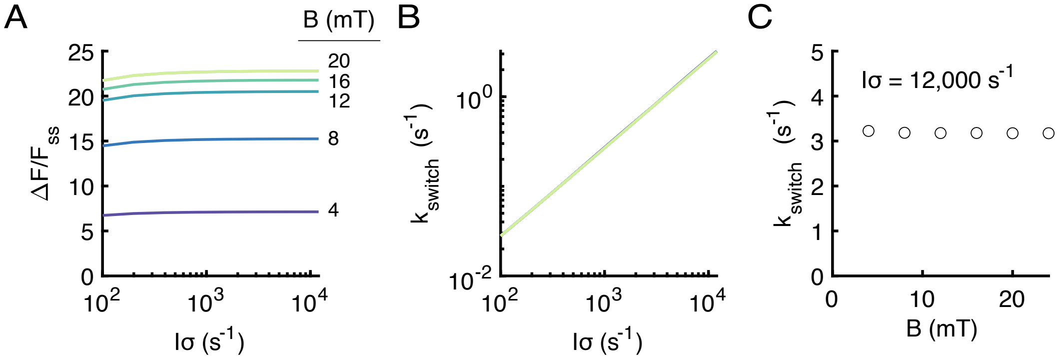

Figure S6. Predicted effect of varying the magnetic field on the MFE in *E. coli*.
Numerical simulations of A) MFE amplitude (compare to Fig. 1E), B) MFE switching kinetics (compare to Fig. 1G), and C) MFE switching rate at $I\sigma$ = 12,000 s^{-1} (compare to Fig. 1H). For these simulations, we used the parameters determined by fitting the *E. coli* data: [$FMNH_2$] = 0.38 µM, [FMN] = 6 µM, η = 3, and β_0 = 0.62. The magnetic fields (B = 4, 8, 12, 16, 20 mT) corresponded to $\beta(B)$ = 0.67, 0.73, 0.78, 0.8, and 0.81.

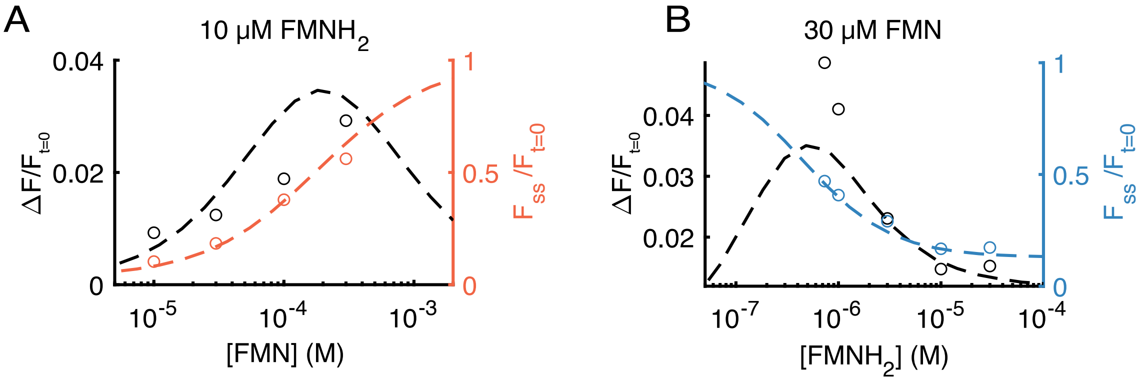

Figure S7. Predicted effects of varying flavin concentrations on the MFE *in vitro*.
Numerical model prediction (dashed lines) for the absolute MFE (data: black circles) and the fractional quenching (data: orange and blue circles) as a function of the concentration of A) FMN (10 µM $FMNH_2$), B) $FMNH_2$ (30 µM FMN). Data are from Figs. 4G, H.

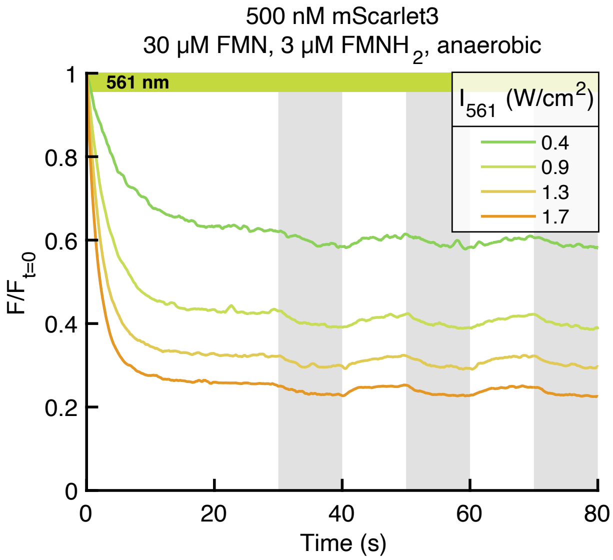

Figure S8. Effect of illumination intensity on MFE in purified mScarlet3.
Higher intensity light led to larger initial quenching, faster MFE switching, and larger relative MFE, $\Delta F/F_{ss}$. Samples were prepared under the same conditions as in Figs. 4G, H.

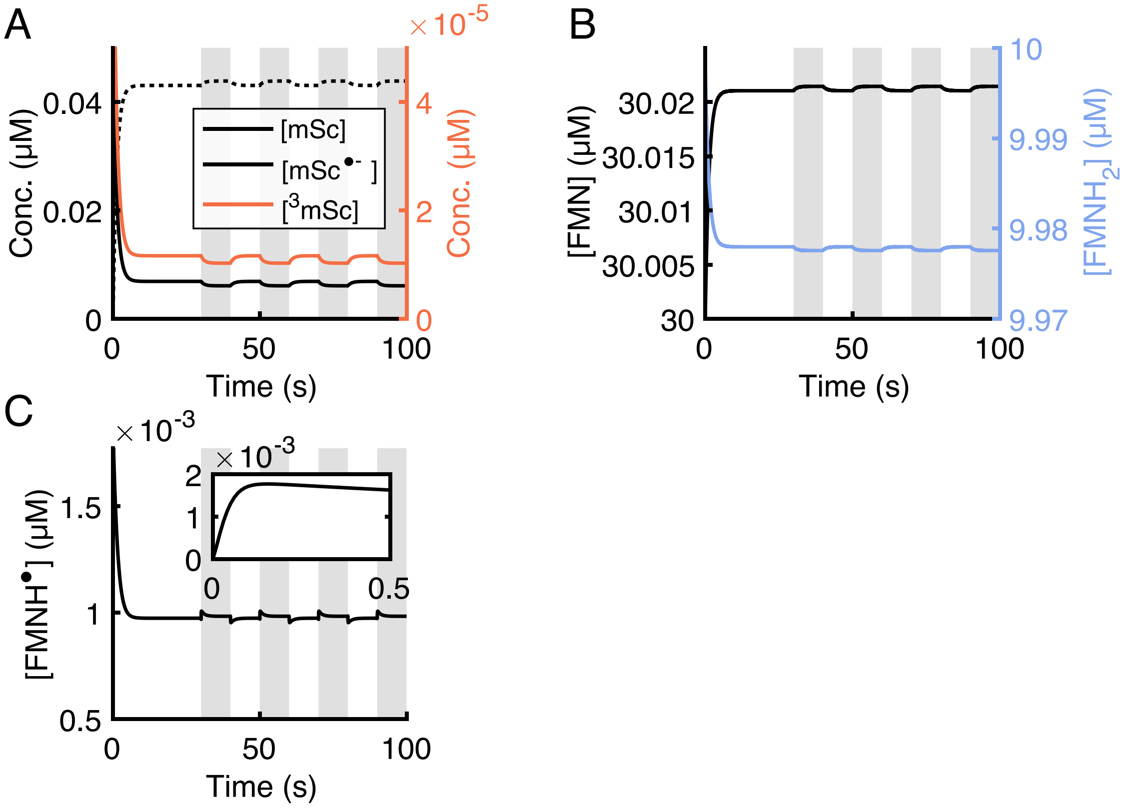

Figure S9. Predicted MFE in photocycle intermediates.

Simulated kinetic traces of mScarlet3 and flavin species. Initial mScarlet3 at 50 nM, FMN at 30 µM, $FMNH_2$ at 10 µM. A) Upon onset of mScarlet3 photo-excitation ($I\sigma = 1652\ s^{-1}$, 1.7 W/cm^2), ground state mScarlet3 rapidly quenches while mSc$^{\bullet-}$ increases. Most mScarlet3 is in these two states; here 0.1% is in the triplet state, ^{3}mSc. B) FMN and $FMNH_2$ concentrations reach a steady-state on the same timescale as the quenching, and show a small MFE since they are in excess of mScarlet3. C) FMNH$^{\bullet}$ concentration shows a small two-component response to the magnetic field. Inset: fast initial dynamics of FMNH$^{\bullet}$ upon production and subsequent separation of the SCRP.

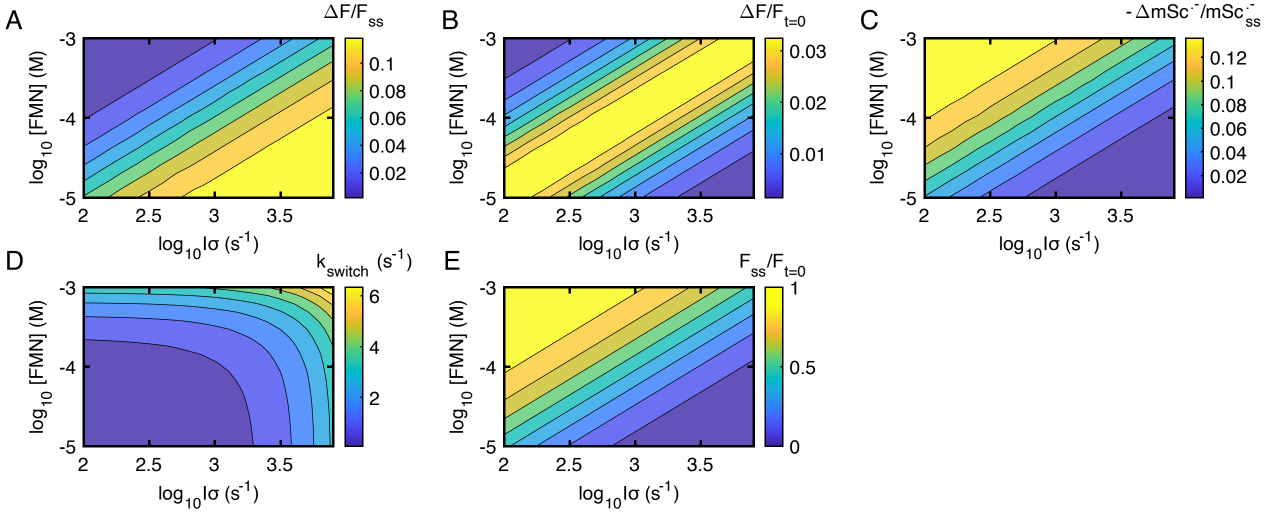

Figure S10. Predicted dependence of MFE photophysics on illumination intensity and [FMN]. Contour plots of A) $\Delta F/F_{ss}$, B) $\Delta F/F_{t=0}$, C) $-\Delta mSc^{\bullet -}/mSc^{\bullet -}_{ss}$, D) k_{switch} for the MFE upstroke, and E) $F_{ss}/F_{t=0}$ as a function of [FMN] and light intensity. Here $[FMNH_2]$ = 10 μM.

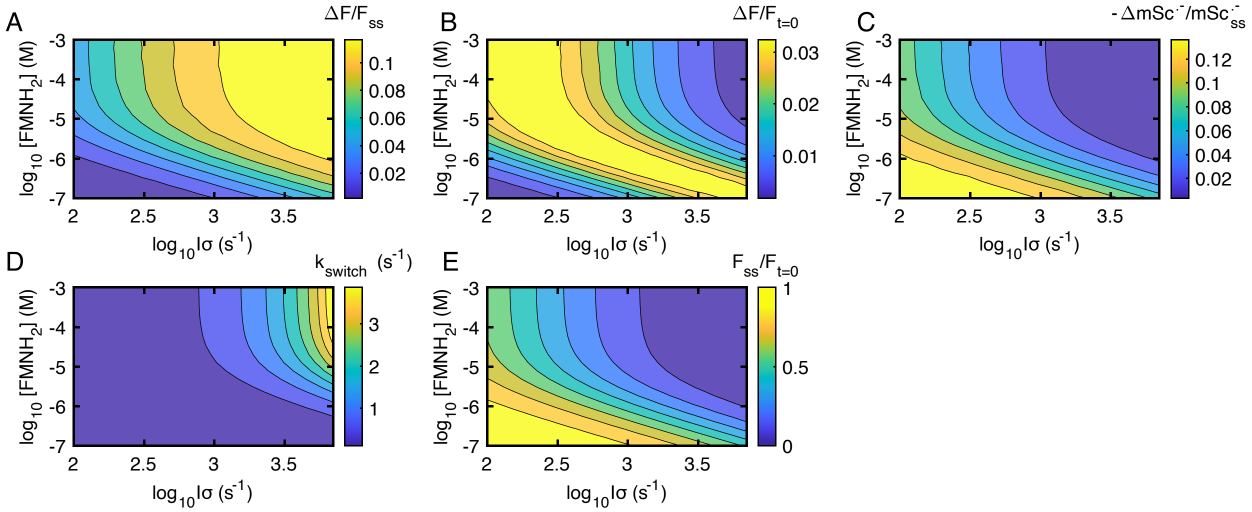

Figure S11. Predicted dependence of MFE photophysics on illumination intensity and $[FMNH_2]$. Contour plots of A) $\Delta F/F_{ss}$, B) $\Delta F/F_{t=0}$, C) $-\Delta mSc^{\bullet -}/mSc^{\bullet -}_{ss}$, D) k_{switch} for the MFE upstroke, and E) $F_{ss}/F_{t=0}$ as a function of $[FMNH_2]$ and light intensity. Here [FMN] = 30 μM.

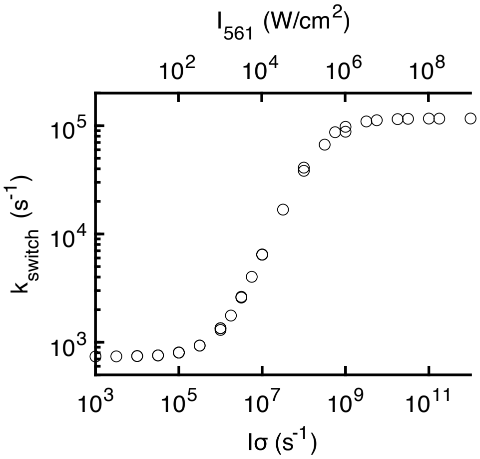

Figure S12. Predicted MFE switching rate *k_{switch}* at high light intensities.
The MFE switching rate (fit to an exponential + constant) increases with light intensity until $I\sigma \approx k_R^S$. Here, [FMN] = 200 mM and [FMNH$_2$] = 1.4 mM, which are the predicted maximal solubilities in water[5,6].

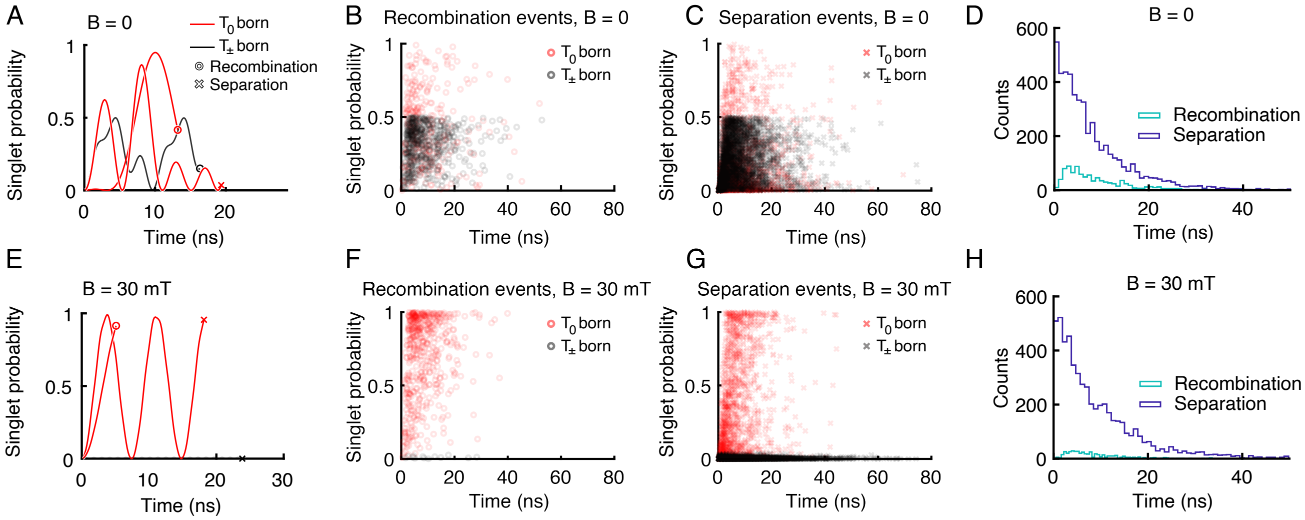

Figure S13. Simulations of spin and chemical dynamics in the SCRP.
A) Representative simulated trajectories of the singlet probability vs. time for a T$_0$ (red) or a T$_\pm$ (black)-born SCRP in zero external magnetic field. Stochastic recombination (circle) and separation (x) events terminate the SCRP. Here $\eta = 1$ and $k_{rec} = 10^8$ s^{-1}. The hyperfine fields were modeled as static, Gaussian-distributed, three-dimensional magnetic fields with standard deviations at each spin $\sigma_1 = \sigma_2 = 2$ mT. B, C) Distribution of recombination (B) and separation (C) events for T$_0$ and T$_\pm$ born SCRPs. D) Simulated rates of recombination (aqua) and separation (purple) vs. time. 2000 SCRPs were initialized in each triplet sublevel. E–H) Same as A–D), but with B = 30 mT.

Modeling of the MFE in mScarlet3

1 Photocycle of mScarlet3/FMN/FMNH$_2$

The following chemical reactions describe the model in main text Fig. 6A:

$$\mathrm{mSc} + h\nu \underset{k_R^{\mathrm{S}}}{\overset{\mathrm{I}\sigma}{\rightleftharpoons}} \mathrm{mSc}^* \tag*{\{1\}}$$

$$\mathrm{mSc}^* \xrightarrow{k_{\mathrm{ISC}}} {}^3\mathrm{mSc} \tag*{\{2\}}$$

$${}^3\mathrm{mSc} \xrightarrow{k_R^{\mathrm{T}}} \mathrm{mSc} \tag*{\{3\}}$$

$${}^3\mathrm{mSc} + \mathrm{FMNH_2} \xrightarrow{k_{\mathrm{red}}} {}^3\mathrm{SCRP} \tag*{\{4\}}$$

$$\mathrm{SCRP} \xrightarrow{k_{\mathrm{sep}}} \mathrm{mSc}^{\bullet -} + \mathrm{FMNH}^{\bullet} \tag*{\{5\}}$$

$${}^1\mathrm{SCRP} \xrightarrow{k_{\mathrm{rec}}} \mathrm{mSc} + \mathrm{FMNH_2} \tag*{\{6\}}$$

$$\mathrm{mSc}^{\bullet -} + \mathrm{FMN} \xrightarrow{k_{\mathrm{ox}}} \mathrm{mSc} + \mathrm{FMNH}^{\bullet} \tag*{\{7\}}$$

$$\mathrm{FMNH}^{\bullet} + \mathrm{FMNH}^{\bullet} \xrightarrow{k_{\mathrm{dis}}} \mathrm{FMN} + \mathrm{FMNH_2} \tag*{\{8\}}$$

In Reaction 5, we assumed that the rate of separation is the same in ^{3}SCRP and ^{1}SCRP while in Reaction 6 we assumed that recombination occurs only from ^{1}SCRP. The magnetic field-dependent $^3\mathrm{SCRP} \iff {}^1\mathrm{SCRP}$ intersystem crossing is analyzed in Section 4.

Since we are interested in dynamics on timescales long compared to the [mSc*] lifetime (4 ns), we make the simplifying approximation $\frac{d[\mathrm{mSc}^*]}{dt} \approx 0 \approx I\sigma[\mathrm{mSc}] - (k_R^{\mathrm{S}} + k_{\mathrm{ISC}})[\mathrm{mSc}^*]$. Thus, $[\mathrm{mSc}^*] \approx \frac{I\sigma}{k_{\mathrm{ISC}}+k_R^{\mathrm{S}}}[\mathrm{mSc}]$, and upon onset of illumination the initial concentration of [mSc] is $[\mathrm{mSc}](t = 0^+) = \left(\frac{k_R^{\mathrm{S}}+k_{\mathrm{ISC}}}{k_R^{\mathrm{S}}+k_{\mathrm{ISC}}+I\sigma}\right)[\mathrm{mSc}^{\mathrm{Tot}}]$, where $[\mathrm{mSc}^{\mathrm{Tot}}]$ is the total concentration of mScarlet3.

Reactions 1 and 2 then simplify to:

$$\mathrm{mSc} + h\nu \underset{k_R^{\mathrm{T}}}{\overset{\mathrm{k}_{\mathrm{ISC}}^{\mathrm{eff}}}{\rightleftharpoons}} {}^3\mathrm{mSc}, \tag*{\{9\}}$$

where

$$k_{\mathrm{ISC}}^{\mathrm{eff}} = \frac{I\sigma\ k_{\mathrm{ISC}}}{k_{\mathrm{ISC}} + k_R^{\mathrm{S}}}$$

is the effective rate from [mSc] into the triplet state [^{3}mSc]. The kinetic equations are then:

$$
\begin{aligned}
\frac{d[\mathrm{mSc}]}{dt} &= -k_{\mathrm{ISC}}^{\mathrm{eff}}[\mathrm{mSc}] + k_R^{\mathrm{T}}[{}^3\mathrm{mSc}] + k_{\mathrm{rec}}[{}^1\mathrm{SCRP}] + k_{\mathrm{ox}}[\mathrm{FMN}][\mathrm{mSc}^{\bullet -}] \\
\frac{d[{}^3\mathrm{mSc}]}{dt} &= +k_{\mathrm{ISC}}^{\mathrm{eff}}[\mathrm{mSc}] - \left(k_R^{\mathrm{T}} + k_{\mathrm{red}}[\mathrm{FMNH_2}]\right)[{}^3\mathrm{mSc}] \\
\frac{d[{}^3\mathrm{SCRP}]}{dt} &= k_{\mathrm{red}}[{}^3\mathrm{mSc}][\mathrm{FMNH_2}] - k_{\mathrm{sep}}[{}^3\mathrm{SCRP}] + \ \ldots \\
\frac{d[{}^1\mathrm{SCRP}]}{dt} &= -(k_{\mathrm{sep}} + k_{\mathrm{rec}})[{}^1\mathrm{SCRP}] + \ \ldots \\
\frac{d[\mathrm{mSc}^{\bullet -}]}{dt} &= k_{\mathrm{sep}}[\mathrm{SCRP}] - k_{\mathrm{ox}}[\mathrm{FMN}][\mathrm{mSc}^{\bullet -}] \\
\frac{d[\mathrm{FMN}]}{dt} &= -k_{\mathrm{ox}}[\mathrm{FMN}][\mathrm{mSc}^{\bullet -}] + k_{\mathrm{dis}}[\mathrm{FMNH}^{\bullet}]^2 \\
\frac{d[\mathrm{FMNH_2}]}{dt} &= -k_{\mathrm{red}}[{}^3\mathrm{mSc}][\mathrm{FMNH_2}] + k_{\mathrm{rec}}[{}^1\mathrm{SCRP}] + k_{\mathrm{dis}}[\mathrm{FMNH}^{\bullet}]^2 \\
\frac{d[\mathrm{FMNH}^{\bullet}]}{dt} &= k_{\mathrm{sep}}[\mathrm{SCRP}] - 2k_{\mathrm{dis}}[\mathrm{FMNH}^{\bullet}]^2 + k_{\mathrm{ox}}[\mathrm{FMN}][\mathrm{mSc}^{\bullet -}].
\end{aligned}
$$

The ellipses in the SCRP reactions indicate that we have omitted intersystem crossing between SCRP singlet and triplet states. We did this because the coherent spin dynamics cannot be described exactly by simple rate equations.

In our model, the spin dynamics in the SCRP act only through their effect on the fraction of SCRPs which separate, $0 \leq \beta(B) \leq 1$, and the fraction which recombine, $1-\beta(B)$. If one takes $\beta(B)$ as a fitting parameter, then it is not necessary to model the SCRP dynamics. We assume the SCRP concentration reaches steady state quickly compared to the changes in [mSc], so $\frac{d[\mathrm{SCRP}]}{dt} \approx 0$. Then the combined mass flux out of the SCRP states must equal the mass flux in from reaction of [$\mathrm{FMNH_2}$] with [^{3}mSc]. This scenario is illustrated in Fig. S14.

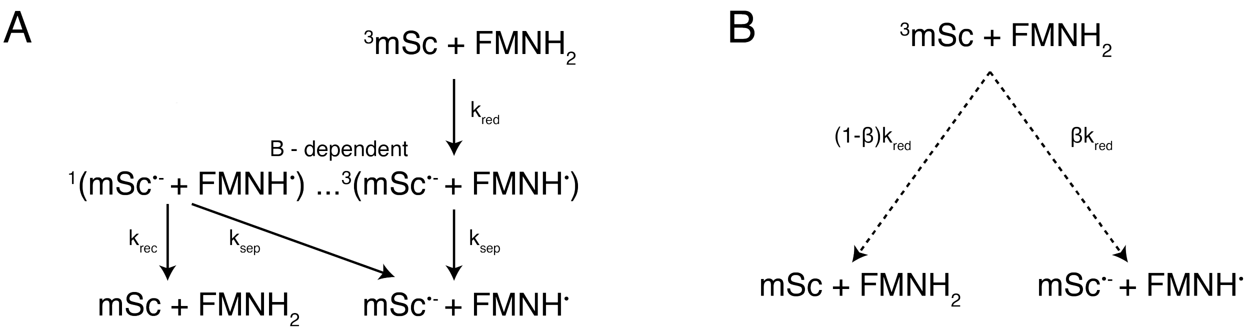

Figure S14: Constructing a simplified model of SCRP dynamics. A) Triplet mScarlet3 reacts with $\mathrm{FMNH_2}$ with rate constant k_{red} to create a triplet-born SCRP (equally populating all three triplet sublevels). The singlet SCRP recombines with rate constant k_{rec}. Both the singlet and the triplet SCRP separate with rate constant $k_{\mathrm{sep.}}$ **B)** The dynamics in **A)** are simplified to a magnetically tuned two-way branch directly from ^{3}mSc + $\mathrm{FMNH_2}$ to the separation or recombination products.

The rate equations are then as below.

$$\frac{d[\mathrm{mSc}]}{dt} = -k_{\mathrm{ISC}}^{\mathrm{eff}}[\mathrm{mSc}] + \left(k_R^{\mathrm{T}} + (1-\beta)k_{\mathrm{red}}[\mathrm{FMNH_2}]\right)[^3\mathrm{mSc}] + k_{\mathrm{ox}}[\mathrm{FMN}][\mathrm{mSc}^{\bullet -}] \tag{1}$$

$$\frac{d[^3\mathrm{mSc}]}{dt} = k_{\mathrm{ISC}}^{\mathrm{eff}}[\mathrm{mSc}] - k_R^{\mathrm{T}}[^3\mathrm{mSc}] - k_{\mathrm{red}}[\mathrm{FMNH_2}][^3\mathrm{mSc}] \tag{2}$$

$$\frac{d[\mathrm{mSc}^{\bullet -}]}{dt} = \beta k_{\mathrm{red}}[\mathrm{FMNH_2}][^3\mathrm{mSc}] - k_{\mathrm{ox}}[\mathrm{FMN}][\mathrm{mSc}^{\bullet -}] \tag{3}$$

$$\frac{d[\mathrm{FMN}]}{dt} = -k_{\mathrm{ox}}[\mathrm{FMN}][\mathrm{mSc}^{\bullet -}] + k_{\mathrm{dis}}[\mathrm{FMNH}^{\bullet}]^2 \tag{4}$$

$$\frac{d[\mathrm{FMNH_2}]}{dt} = -\beta k_{\mathrm{red}}[\mathrm{FMNH_2}][^3\mathrm{mSc}] + k_{\mathrm{dis}}[\mathrm{FMNH}^{\bullet}]^2 \tag{5}$$

$$\frac{d[\mathrm{FMNH}^{\bullet}]}{dt} = \beta k_{\mathrm{red}}[^3\mathrm{mSc}][\mathrm{FMNH_2}] - 2k_{\mathrm{dis}}[\mathrm{FMNH}^{\bullet}]^2 + k_{\mathrm{ox}}[\mathrm{FMN}][\mathrm{mSc}^{\bullet -}]. \tag{6}$$

These equations are simulated in the Supplementary Code in `MFE_kinetic_model.m` via MATLAB's `ode23s` solver. The rate constants $k_R^{\mathrm{T}}, k_{\mathrm{ISC}}, k_{\mathrm{red}}$ and k_{ox}, and the parameter $\beta(B)$ are fit via the steps in Section 2. The rate constants k_R^{S} and k_{dis} are taken from the literature.

2 Model fitting

2.1 Two-state approximation

To fit our model, we determine an analytical form for the dependence of the recovery and quenching rates on [FMN] and [$\mathrm{FMNH_2}$] (Fig. 6B–E). We make the approximations $[\mathrm{FMN}] \gg [\mathrm{mSc}^{\mathrm{Tot}}]$ and $[\mathrm{FMNH_2}] \gg [\mathrm{mSc}^{\mathrm{Tot}}]$. These approximations are not universal, but do correspond to the conditions of our *in vitro* experiments, where both flavin concentrations were at least 10-fold greater than [$\mathrm{mSc}^{\mathrm{Tot}}$]. Under these approximations, Eq. 2 becomes:

$$\frac{d[^3\mathrm{mSc}]}{dt} \approx 0 \approx k_{\mathrm{ISC}}^{\mathrm{eff}}[\mathrm{mSc}] - k_R^{\mathrm{T}}[^3\mathrm{mSc}] - k_{\mathrm{red}}[\mathrm{FMNH_2}][^3\mathrm{mSc}].$$

Thus $[^3\mathrm{mSc}] = \chi[\mathrm{mSc}]$, with:

$$\chi \equiv \frac{k_{\mathrm{ISC}}^{\mathrm{eff}}}{k_R^{\mathrm{T}} + k_{\mathrm{red}}[\mathrm{FMNH_2}]}.$$

Then, we can simplify the mScarlet3 dynamics to a two-state model:

$$\frac{d[\mathrm{mSc}]}{dt} = -\chi\beta k_{\mathrm{red}}[\mathrm{FMNH_2}][\mathrm{mSc}] + k_{\mathrm{ox}}[\mathrm{FMN}][\mathrm{mSc}^{\bullet -}]$$

$$\frac{d[\mathrm{mSc}^{\bullet -}]}{dt} = \chi\beta k_{\mathrm{red}}[\mathrm{FMNH_2}][\mathrm{mSc}] - k_{\mathrm{ox}}[\mathrm{FMN}][\mathrm{mSc}^{\bullet -}].$$

The initial quenching rate is the sum of the rates into and out of the mScarlet3 radical anion.

$$\begin{aligned} k_{\text{quench}} &= k_{\text{ox}}[\text{FMN}] + \chi\beta k_{\text{red}}[\text{FMNH}_2] \\ &= k_{\text{ox}}[\text{FMN}] + \frac{\beta k_{\text{ISC}}^{\text{eff}}}{1 + \frac{k_R^{\text{T}}}{k_{\text{red}}[\text{FMNH}_2]}}. \end{aligned} \tag{7}$$

2.2 Fitting the intersystem crossing rate and the triplet lifetime

This section pertains to the fitting in Figure 5.

In the absence of flavins, there is no charge transfer in our model. Only reactions {1}–{3} occur, and rate equations 1–2 apply. These equations simplify to:

$$\begin{aligned} \frac{d[\text{mSc}]}{dt} &= -k_{\text{ISC}}^{\text{eff}}[\text{mSc}] + k_R^{\text{T}}[^3\text{mSc}] \\ \frac{d[^3\text{mSc}]}{dt} &= +k_{\text{ISC}}^{\text{eff}}[\text{mSc}] - k_R^{\text{T}}[^3\text{mSc}]. \end{aligned}$$

We assume the initial conditions $[\text{mSc}(t=0)] = c_0$ and $[^3\text{mSc}(t=0)] = 0$. Then,

$$[\text{mSc}(t)] = \frac{c_0}{k_{\text{ISC}}^{\text{eff}} + k_R^{\text{T}}}\left(k_{\text{ISC}}^{\text{eff}} e^{-(k_{\text{ISC}}^{\text{eff}} + k_R^{\text{T}})t} + k_R^{\text{T}}\right) \tag{8}$$

$$[^3\text{mSc}(t)] = c_0 - [\text{mSc}(t)]. \tag{9}$$

We measured the rate of exponential decay $k_{\text{transient}}$ and the steady-state ratio of triplet to singlet as $t \to \infty$, $\left([^3\text{mSc}]/[\text{mSc}]\right)_{\text{s.s.}}$ for varying light intensities $I\sigma$ (Fig. 5C).

Fig. 5D shows $k_{\text{transient}} = k_{\text{ISC}}^{\text{eff}} + k_R^{\text{T}} = \frac{k_{\text{ISC}}}{k_{\text{ISC}} + k_R^{\text{S}}} I\sigma + k_R^{\text{T}}$, plotted against $I\sigma$. We fit the slope and intercept to determine $\frac{k_{\text{ISC}}}{k_{\text{ISC}} + k_R^{\text{S}}}$ and k_R^{T}. The best-fit value was $k_R^{\text{T}} = 224\,\text{s}^{-1}$. However, $k_{\text{ISC}}^{\text{eff}} \ll k_R^{\text{T}}$ over the range of light intensities we tested. Therefore, the slope is not well-constrained and we cannot determine k_{ISC} from this graph.

Fig. 5E shows $\left([^3\text{mSc}]/[\text{mSc}]\right)_{\text{s.s.}} = \frac{k_{\text{ISC}}^{\text{eff}}}{k_R^{\text{T}}} = \frac{k_{\text{ISC}}}{k_R^{\text{T}}(k_{\text{ISC}} + k_R^{\text{S}})} I\sigma$ against $I\sigma$. We fit the slope, which provides another measure of k_{ISC}, given k_R^{T}. The best-fit value was $k_{\text{ISC}} = 1.9 \times 10^5\ \text{s}^{-1}$.

2.3 Fitting the rates of oxidation and reduction

This section pertains to the fitting in Figs. 6B–E.

After a period of intense yellow illumination to produce $\text{mSc}^{\bullet-}$, we measured the recovery of mSc at constant [FMNH_2], variable [FMN], and magnetic field $B = 0$ (Fig. 4G). In these experiments, we needed to illuminate the sample with some yellow light to monitor the mSc recovery, but we wanted to minimize the dose to avoid driving photochemical production of $\text{mSc}^{\bullet-}$. We compromised by rapidly flickering the yellow light between 0 and 100% at a duty cycle $A = 5\%$.

The rate of [mSc] recovery is similar to the expression for the rate of quenching, Equation 7:

$$k_{\text{recovery}} = k_{\text{ox}}[\text{FMN}] + A\frac{\beta k_{\text{ISC}}^{\text{eff}}}{1+\frac{k_R^{\text{T}}}{k_{\text{red}}[\text{FMNH}_2]}},$$

but here the second term is multiplied by A, the duty cycle of the light. Since $[\text{FMNH}_2]$ was constant for this set of measurements, we plotted the recovery rates as a function of the FMN concentration. The slope was $k_{\text{ox}} = 3375\ \text{M}^{-1}\,\text{s}^{-1}$.

Then, at constant [FMN], constant light intensity, and variable $[\text{FMNH}_2]$ (Fig. 4H), we measured the initial quenching rates. The magnetic field was $B = 0$. We plotted $k_{\text{quench}} - k_{\text{ox}}[\text{FMN}] = \frac{\beta k_{\text{ISC}}^{\text{eff}}}{1+k_R^{\text{T}}/(k_{\text{red}}[\text{FMNH}_2])}$ against $[\text{FMNH}_2]$. We used the best-fit value of k_{ox} from above, and we fit the dependence of the quenching rates on $[\text{FMNH}_2]$ to determine $\beta_0 \equiv \beta(B=0)$ and k_{red}. For $k_{\text{ISC}} = 1.9\times10^5\ \text{s}^{-1}$ and $I\sigma$[1]$= 1652\ \text{s}^{-1}$, the best-fit values were $k_{\text{red}} = 5\times10^7\ M^{-1}s^{-1}$ and $\beta_0 = 0.81$.

2.4 Fitting the SCRP branching ratios

We then fit $\Delta F/F_{\text{ss}}$ and $\Delta F/F_{t=0}$ against [FMN] and $[\text{FMNH}_2]$ and obtained $\beta_{\text{sat}} = 0.93$. We included a constant offset of 3% to the fluorescence to account for background. The mScarlet3 radical anion was nonfluorescent under 561 nm excitation; the fluorescence of the quenched product could be entirely attributed to fluorescence from residual mScarlet3. We allowed the light intensity (measured at $\approx 1.5\ \text{W/cm}^2$) to vary in our model; the best-fit value was $I = 1652\ \text{s}^{-1} = 1.7\ \text{W/cm}^2$.

2.5 Fitting the E. coli data

This section pertains to the fitting in Fig. 6G.

Using the same kinetic parameters as for the purified protein, we 1) determined $[\text{FMNH}_2]$ via the light intensity dependence of the switching rate for the MFE upstroke k_{switch} (Fig. 1G), and 2) determined [FMN] via the steady-state residual fluorescence $F_{ss}/F_{t=0}$ at the lowest light intensity we tested ($I\sigma\ = 145\ s^{-1}$), as follows:

1) The switching rate of the MFE upstroke[2] is a constant plus a linear function of illumination intensity:

$$\begin{aligned} k_{\text{switch}} = k_{\text{quench}} &= k_{\text{ox}}[\text{FMN}] + \frac{\beta k_{\text{ISC}}^{\text{eff}}}{1+\frac{k_R^{\text{T}}}{k_{\text{red}}[\text{FMNH}_2]}} \\ &= k_{\text{ox}}[\text{FMN}] + \frac{\beta I\sigma k_{\text{ISC}}}{(k_R^{\text{S}}+k_{\text{ISC}})(1+\frac{k_R^{\text{T}}}{k_{\text{red}}[\text{FMNH}_2]})}. \end{aligned}$$

We plotted k_{switch} for the upstroke against $I\sigma$. The best-fit slope was $m = 3.13\times10^{-4}$. Using the rate constants from the model fit for the purified protein, we obtained $[\text{FMNH}_2] \approx 6\ \mu\text{M}$. However, the error on the intercept

---

[1] The molar extinction coefficient of mScarlet3 at 561 nm is $\epsilon_{561} = 89{,}440\ M^{-1}\text{cm}^{-1}$ which corresponds to an absorption cross section of $\sigma_{561} = \frac{\ln(10)\ \times10^3}{N_A}\epsilon_{561} = 3.46\ \times 10^{-16}\ \text{cm}^2$.

[2] For a discussion of the switching rate, see Section 3.2.

was too large to determine [FMN].

2) The steady state ratio of bright to dark forms of mScarlet3 is proportional to [FMN]:

$$
\begin{aligned}
F_{ss}/(F_{t=0} - F_{\mathrm{ss}}) &= \left(\frac{[\mathrm{mSc}]}{[\mathrm{mSc}^{\bullet -}]}\right)_{\mathrm{ss}} \\
&= \frac{k_{\mathrm{ox}}[\mathrm{FMN}](1 + \frac{k_R^{\mathrm{T}}}{[k_{\mathrm{red}}[\mathrm{FMNH_2}]})}{\beta k_{\mathrm{ISC}}^{\mathrm{eff}}} \\
&= \frac{k_{\mathrm{ox}}[\mathrm{FMN}]}{I\sigma\ m}
\end{aligned}
$$

where m is the slope determined in step (1) above. Rearranging, $[\mathrm{FMN}] = \frac{I\sigma\ m}{k_{\mathrm{ox}}} \frac{F_{\mathrm{ss}}}{F_{\mathrm{t=0}} - F_{\mathrm{ss}}}$. We performed the fit at the lowest light intensity to reduce the impact of photobleaching on the measurement of F_{ss}. At $I\sigma = 145\ \mathrm{s}^{-1}$, $F_{ss}/(F_{t=0} - F_{\mathrm{ss}}) = 0.03$, implying $[\mathrm{FMN}] \approx 0.38$ μM, consistent with literature values[7].

We adjusted β_0 and β_{sat} in our model to match the maximal amplitude of the relative MFE, $\Delta F/F_{ss}$. While we used β_0 and β_{sat} as fitting parameters, the discussion in Section 4 shows that the differences from *in vitro* can be explained solely by tuning the ratio of SCRP separation and recombination rate constants, η, in Eqs. 12 and 13.

3 Maximizing the MFE sensitivity and kinetics

3.1 MFE amplitude

We seek a formula for the absolute and relative MFE amplitudes, $\Delta F/F_{\mathrm{t=0}}$ and $\Delta F/F_{\mathrm{ss}}$, respectively, in the limit of small $\Delta\beta$. This scenario applies either to small changes in magnetic field or to cases where β_{sat} and β_0 are similar in value (e.g. both are close to 1). Using the approximation from Section 2.1, we write the fractional steady-state residual fluorescence $x \equiv F_{\mathrm{ss}}(\beta)/F_{\mathrm{t=0}}$ as:

$$
\begin{aligned}
x &= \frac{k_{\mathrm{ox}}[\mathrm{FMN}]}{k_{\mathrm{quench}}} \\
&= \frac{k_{\mathrm{ox}}[\mathrm{FMN}]}{k_{\mathrm{ox}}[\mathrm{FMN}] + \frac{\beta k_{\mathrm{ISC}}^{\mathrm{eff}}}{1 + k_R^{\mathrm{T}}/(k_{\mathrm{red}}[\mathrm{FMNH_2}])}} \\
&= \frac{k_R}{k_R + \beta k_F},
\end{aligned}
$$

where we have introduced k_R and k_F to simplify the expression. We take the derivative with respect to β:

$$
\begin{aligned}
\frac{dx}{d\beta} &= \frac{-k_R k_F}{(k_R + \beta k_F)^2} \\
&= -\frac{1}{\beta} x(1 - x).
\end{aligned}
$$

Therefore, in the limit where $\Delta\beta$ is small,

$$\Delta F/F_{t=0} = \frac{\Delta\beta}{\beta}x(1-x)$$
$$\Delta F/F_{\mathrm{ss}} = \frac{\Delta\beta}{\beta}(1-x).$$

(In the main text we defined ΔF to be positive, though the magnetic field decreased fluorescence; and β is a strictly increasing function of B.) These simple relations show that for small MFEs, the absolute and relative MFE amplitudes follow universal curves, parameterized by the fractional steady-state residual fluorescence $x \equiv F_{\mathrm{ss}}(\beta)/F_{\mathrm{t=0}}$.

3.2 MFE switching kinetics

Upon a change in the magnetic field, the fluorescence reaches a new steady-state, F_{ss}. At low light intensities, ($I\sigma \lesssim 10^6$ s^{-1} so the fractional population of ^{3}mSc is small):

$$k_{\text{switch (upstroke)}} = k_{\text{quench}}(\beta_0) \tag{10}$$
$$k_{\text{switch (downstroke)}} = k_{\text{quench}}(\beta_{\mathrm{sat}}). \tag{11}$$

k_{quench} and thus k_{switch} are linearly dependent on [FMN] and $I\sigma$, and also depend on [FMNH$_2$] up to $k_R^{\mathrm{T}}/k_{\mathrm{red}}$ (Equation 7) which is ≈ 4 µM. Therefore, to increase the MFE switching rate, one should increase the light intensity and flavin concentrations. However, increasing [FMN] will increase $F_{\mathrm{ss}}/F_{\mathrm{t=0}}$, while increasing the light intensity or [FMNH$_2$] will decrease it.

At high light intensities, the initial quenching dynamics change. Upon high-intensity illumination, a substantial portion of the initial fluorescence quenching comes from populating photocycle intermediates — the mScarlet3 triplet state ^{3}mSc (at $I\sigma \gtrsim 10^6$ s^{-1})[3] and the excited state, mSc* (at $I\sigma \gtrsim 10^8$ s^{-1}).

Our simulations of the switching as a function of light intensity in Fig. S12 explicitly track the excited state, [mSc*] and fit the upstroke switching rate. The range of $I\sigma$ over which Eqs. 10–11 hold depends on [FMNH$_2$], since the rate out of the mScarlet3 triplet state is [FMNH$_2$]-dependent.

4 Intersystem crossing in the SCRP

The details of the SCRP dynamics can be modeled at different levels of theory, though our data do not probe these dynamics directly. The branching fraction $\beta(B)$ depends on the coherent spin dynamics within the SCRP, and also on the rate constants for separation (assumed to be equal for the singlet and triplet states), and for recombination (assumed to be nonzero only in the singlet state). Below we first summarize the predictions of

---

[3] For example, at $I\sigma = 10^6$ s^{-1}, [FMN] = 30 µM, [FMNH$_2$] = 10 µM, the simulated dynamics are significantly different from what we observed in experiments. The approximation in Section 2.1 no longer holds. During the initial drop in fluorescence, [^{3}mSc] builds up. [^{3}mSc]/[mSc$^{\mathrm{Tot}}$] peaks at 40% and then ^{3}mSc slowly converts to mSc$^{\bullet -}$. The timescale of this conversion is slightly faster compared to the MFE switching rate at this light intensity, thus the quenching is described by a multiexponential. Subsequent switching events after a long time are accompanied by smaller variations in ^{3}mSc.

a kinetic model of the SCRP dynamics from Hayashi and Nagakura. Then we present a calculation that takes into accounts for the time evolution of individual SCRP.

4.1 Rate-based model of SCRP dynamics

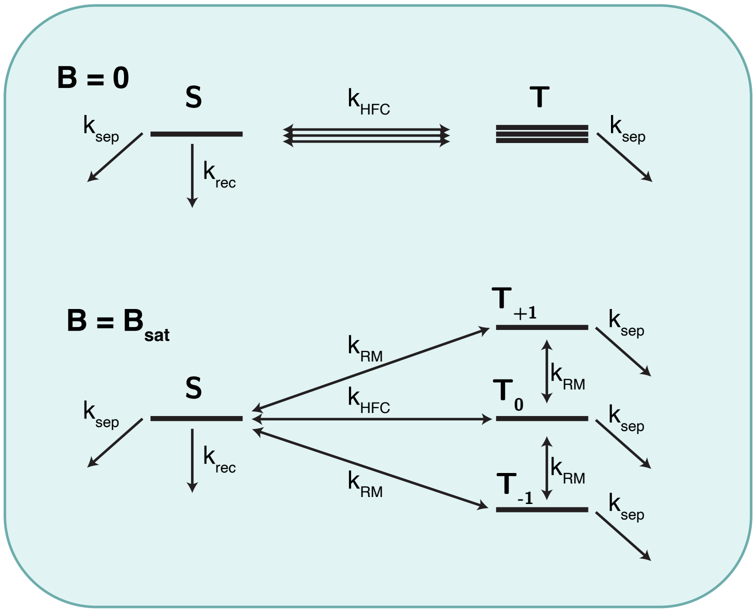

Figure S15: Model of SCRP interconversion with first-order rates. At zero magnetic field, coherent interconversion (k_{HFC}) between S and T states drives hyperfine mixing. At saturating magnetic field, the $T_{\pm}$ states only interconvert with S or T_0 through incoherent processes (rate constant k_{RM}).

Hayashi and Nagakura proposed a rate-based model of SCRP dynamics which takes into account a finite rate of intersystem crossing, as well as relaxation between the triplet sublevels, as in Fig. S15[8]. This model only considers the limits of zero and strong magnetic field. In the absence of magnetic field, all three triplet sublevels interconvert with S with rate constant k_{HFC}. In the presence of a saturating magnetic field, the $\mathrm{T}_{\pm}$ sublevels interconvert with S and with T_0 with rate constant $k_{\mathrm{RM}} \ll k_{\mathrm{HFC}}$, while T_0 and S continue to interconvert with rate constant k_{HFC}, which is unaffacted by magnetic field[8–10].

We assume that the SCRP is triplet-born, and that initially the three triplet sublevels are equally populated. We apply the steady-state approximation ($\frac{d[\mathrm{S}]}{dt}, \frac{d[\mathrm{T}_-]}{dt}, \frac{d[\mathrm{T}_0]}{dt}, \frac{d[\mathrm{T}_+]}{dt} \approx 0$), and solve for β in zero magnetic field:

$$\beta_0 = \frac{k_{\mathrm{sep}}\left(2k_{\mathrm{HFC}} + k_{\mathrm{rec}} + k_{\mathrm{sep}}\right)}{k_{\mathrm{HFC}}\left(k_{\mathrm{rec}} + 2k_{\mathrm{sep}}\right) + k_{\mathrm{sep}}\left(k_{\mathrm{rec}} + k_{\mathrm{sep}}\right)}.$$

In the limit of high k_{HFC} relative to k_{rec} and k_{sep} this expression becomes:

$$\beta_0 \approx \frac{2k_{\mathrm{sep}}}{k_{\mathrm{rec}} + 2k_{\mathrm{sep}}}. \tag{12}$$

Introducing the parameter $\eta \equiv k_{\mathrm{rec}}/k_{\mathrm{sep}}$, Eq. 12 becomes $\beta_0 = \frac{1}{1+\eta/2}$.

In saturating magnetic field, the same calculation gives:

$$\beta_{\text{sat}} = \frac{k_{\text{sep}}\left(3k_{\text{sep}}\left(2k_{\text{HFC}} + k_{\text{rec}} + 6k_{\text{RM}}\right) + 2k_{\text{rec}}\left(k_{\text{HFC}} + 5k_{\text{RM}}\right) + 24k_{\text{RM}}\left(k_{\text{HFC}} + k_{\text{RM}}\right) + 3k_{\text{sep}}^2\right)}{3\left(k_{\text{sep}}^2\left(2k_{\text{HFC}} + k_{\text{rec}} + 6k_{\text{RM}}\right) + k_{\text{sep}}\left(k_{\text{rec}}\left(k_{\text{HFC}} + 4k_{\text{RM}}\right) + 8k_{\text{RM}}\left(k_{\text{HFC}} + k_{\text{RM}}\right)\right) + 2k_{\text{rec}}k_{\text{RM}}\left(k_{\text{HFC}} + k_{\text{RM}}\right) + k_{\text{sep}}^3\right)}.$$

In the limit of small k_{RM} and large k_{HFC} relative to k_{rec} and k_{sep}, this expression becomes:

$$\beta_{\text{sat}} \approx \frac{2}{3} + \frac{2k_{\text{sep}}}{3(k_{\text{rec}} + 2k_{\text{sep}})}. \tag{13}$$

Combining Eqs. 12 and 13 gives an extremely simple relation between β_0 and β_{sat}:

$$\beta_{\text{sat}} \approx \frac{2}{3} + \frac{1}{3}\beta_0. \tag{14}$$

Thus β_0 and β_{sat} cannot be selected independently. Rather, these two quantities lie on a single curve, parameterized by η. The variable η is a function of classical rate constants, which could be tuned, e.g. by adjusting solvent viscosity or polarity, or by altering the charge or hydrophobicity of the reactants.

The major limitations of the model of Hayashi and Nagakura are: (1) it does not interpolate smoothly to intermediate values of B, and (2) the use of classical rate constants to describe coherent intersystem crossing does not capture the non-exponential spin dynamics.

4.2 SCRP spin and chemical reaction simulations

Single spin and two spin simulations

In the MATLAB script `SCRP_spin_sim.m`, we numerically simulate the time evolution for a single spin in an arbitrary magnetic field $\mathbf{B}$ and for a pair of spins S_1 and S_2 in fields $\mathbf{B}_1$ and $\mathbf{B}_2$.

A single electron spin in a magnetic field $\mathbf{B}$ undergoes Larmor precession. The Hamiltonian is $H = g\mu_B(\mathbf{B}\cdot\mathbf{S})/\hbar$, where g is the Landé g-factor, $\mu_B = 9.3 \times 10^{-24}$ J/T is the Bohr magneton, and $\mathbf{S} = \frac{\hbar}{2}\boldsymbol{\sigma}$ where $\boldsymbol{\sigma}$ is the vector of Pauli spin matrices. The time-evolution operator is $U(t) = e^{-iHt/\hbar}$, and the spin evolves via $\psi(t) = U(t)\psi_0$.

$$U(t) = \begin{bmatrix} \cos(\omega t/2) + ib_z\sin(\omega t/2) & (ib_x + b_y)\sin(\omega t/2) \\ (ib_x - b_y)\sin(\omega t/2) & \cos(\omega t/2) - ib_z\sin(\omega t/2) \end{bmatrix}, \tag{15}$$

where $\omega = g\mu_B|\mathbf{B}|/\hbar$, and $b_i = \mathbf{B}\cdot\hat{\mathbf{i}}/|\mathbf{B}|$. The probability of being in the state $|\uparrow\rangle$, for example, at time t, is $|\langle\uparrow|\psi(t)\rangle|^2$.

Two electron spins span a four-dimensional state space. The vectors $|\uparrow\uparrow\rangle, |\uparrow\downarrow\rangle, |\downarrow\uparrow\rangle, |\downarrow\downarrow\rangle$ form a basis:

$$|\uparrow\uparrow\rangle = \begin{pmatrix}1\\0\\0\\0\end{pmatrix};\ |\uparrow\downarrow\rangle = \begin{pmatrix}0\\1\\0\\0\end{pmatrix};\ |\downarrow\uparrow\rangle = \begin{pmatrix}0\\0\\1\\0\end{pmatrix};\ |\downarrow\downarrow\rangle = \begin{pmatrix}0\\0\\0\\1\end{pmatrix}.$$

The singlet and triplet states are:

$$\underbrace{\frac{1}{\sqrt{2}}(|{\uparrow\downarrow}\rangle - |{\downarrow\uparrow}\rangle) = \frac{1}{\sqrt{2}}\begin{pmatrix}0\\1\\1\\0\end{pmatrix};}_{\text{singlet state}} \quad \underbrace{\frac{1}{\sqrt{2}}(|{\uparrow\downarrow}\rangle + |{\downarrow\uparrow}\rangle) = \frac{1}{\sqrt{2}}\begin{pmatrix}0\\1\\-1\\0\end{pmatrix};\; |{\uparrow\uparrow}\rangle = \begin{pmatrix}1\\0\\0\\0\end{pmatrix};\; |{\downarrow\downarrow}\rangle = \begin{pmatrix}0\\0\\0\\1\end{pmatrix}}_{\text{triplet states}}.$$

The Hamiltonian is $H = -g\mu_B(\mathbf{B}_1 \cdot \mathbf{S}_1 + \mathbf{B}_2 \cdot \mathbf{S}_2)/\hbar$ where $\mathbf{S}_1$ and $\mathbf{S}_2$ are the spin operators for spins 1 and 2, in the new basis. The components are $S_{1x} = S_x \otimes I_2$, ... $S_{2x} = I_2 \otimes S_x$, etc., where $S_{\{x,y,z\}} = \frac{\hbar}{2}\sigma_{\{x,y,z\}}$ and I_2 is the 2×2 identity matrix.

We numerically compute the wavefunction $\psi(t) = U(t)\,|\psi_0\rangle$ with $U(t) = e^{-iHt/\hbar}$. For initial conditions, ψ_0 is drawn from the T_0, T_+, or T_- states. We determine the corresponding singlet and triplet amplitudes and probabilities at each time, e.g., for the singlet probability, $p_S(t) = |\,\langle S|U|\psi_0\rangle\,|^2$.

Analytical derivations for two-spin singlet and triplet probabilities

An alternative approach is to obtain the analytical expressions for the singlet and triplet probabilities given magnetic fields $\mathbf{B}_1$ and $\mathbf{B}_2$. In the Mathematica notebook `spin_dynamics.nb`, we derive $p_S(t)$, $p_{T_0}(t)$, and $p_{T_\pm}(t)$, for an SCRP born in either the T_0 state or the T_+ state. T_- and T_+-born SCRPs have the same expressions but with the substitution $p_{T_+} \leftrightarrow p_{T_-}$. These expressions agree with the results from numerical simulations above.

For two electron spins that are non-interacting, $\langle\psi_f|U_{\text{tot}}|\psi_{0,tot}\rangle = \langle\psi_f|U|\psi_0\rangle_1\,\langle\psi_f|U|\psi_0\rangle_2$ where the subscript outside the brackets indicates spin 1 or spin 2. The singlet state is $\frac{1}{\sqrt{2}}(|{\uparrow\downarrow}\rangle - |{\downarrow\uparrow}\rangle)$, and the triplet states T_0, T_+, and T_- are $\frac{1}{\sqrt{2}}(|{\uparrow\downarrow}\rangle + |{\downarrow\uparrow}\rangle)$, $|{\uparrow\uparrow}\rangle$, and $|{\downarrow\downarrow}\rangle$. The first arrow indicates spin 1 and the second indicates spin 2.

For example, the singlet probability for a T_+-born spin state at time t is $|\,\langle S|U_{\text{tot}}|T_+\rangle\,|^2$ where:

$$\begin{aligned}\langle S|U_{\text{tot}}|T_+\rangle &= \frac{1}{\sqrt{2}}\big(\langle{\uparrow\downarrow}|\,U_{tot}\,|{\uparrow\uparrow}\rangle - \langle{\downarrow\uparrow}|\,U_{tot}\,|{\uparrow\uparrow}\rangle\big)\\ &= \frac{1}{\sqrt{2}}\big(\langle\uparrow|U|\uparrow\rangle_1\,\langle\downarrow|U|\uparrow\rangle_2 - \langle\downarrow|U|\uparrow\rangle_1\,\langle\uparrow|U|\uparrow\rangle_2\big),\end{aligned}$$

where U is the same as in Equation 15.

Spin and chemical dynamics simulations

In the MATLAB script `SCRP_spin_and_chem_sim.m`, we simulate the full quantum dynamics of the SCRP, including the chemical dynamics, to obtain $\beta(B)$ for arbitrary B. The treatment below closely follows Refs. 11, 12.

We simulated the time-evolution of the spins using the methods above. We assumed that the SCRPs are born with equal probabilities in states T_0, T_+, or T_-. We further assumed that the dominant driver of intersystem crossing is hyperfine coupling to nearby magnetically active nuclei; that exchange and dipolar interactions between the two spins are negligible; that spin-orbit coupling is negligible; and that the Landé g-factor is isotropic and equal for both spins. We assumed that all reaction dynamics are fast compared to incoherent spin relaxation mechanisms, i.e. we ignored processes with rate constant k_{RM} in the Hayashi and Nagakura model. Each electron spin in the SCRP is subject to a distinct, approximately static, hyperfine field ($\mathbf{B}_1$, $\mathbf{B}_2$). We drew each component $B_{1x}, B_{1y}, B_{1z}; B_{2x}, B_{2y}, B_{2z}$ from normal distributions with standard deviations σ_1 and σ_2, respectively. A constant and homogeneous external magnetic field was added, so for spin j, $B_{jz,\mathrm{tot}} = B_{jz} + B_{\mathrm{ext}}$.

For each SCRP, we ran the simulation until the SCRP reacted, either via separation or recombination. At each time-step, we calculated the separation and recombination probabilities, and used a random number generator to determine which, if either, event occurred. The probability of separation was independent of the spin state, so $p_{\mathrm{sep}} = k_{\mathrm{sep}}\Delta t$, where Δt is the time step. The probability of recombination was proportional to the singlet probability, so $p_{\mathrm{rec}} = k_{\mathrm{rec}}(1 - \alpha(t))\Delta t$, where $\alpha(t)$ is the triplet probability at time t.

We simulated the spin and reaction dynamics of each individual SCRP (Fig. S13) before taking the ensemble average over embodiments of the hyperfine fields. This ordering of simulation steps was important because spin-dependent reactivity could alter the statistical distribution of the hyperfine fields of the surviving SCRPs, altering the ensemble dynamics. We counted the fraction of molecules that separated to determine $\beta(B)$.

We used $k_{\mathrm{rec}} = 10^8$ s^{-1} and varied $\eta \equiv k_{\mathrm{sep}}/k_{\mathrm{rec}}$ from 0.1 to 100. We assumed that $\sigma_1 = \sigma_2 = 2$ mT. We varied B_{ext} from 0 to 30 mT; for β_{sat} in Fig. 7J we used B_{ext} = 300 mT. For each value of B_{ext} and η, we simulated $5 \cdot 10^3$ SCRPs starting in each of T_0, T_+, and T_-. This approach yields the full function $\beta(B)$, and allows us to vary $\eta = k_{\mathrm{sep}}/k_{\mathrm{rec}}$ without making assumptions about the timescales of the kinetic rate constants compared to the spin dynamics.

In the absence of chemical reactions, the S, T_0, and $T_\pm$ dynamics are non-exponential, following the distributions in Refs. 11, 12. In zero external field, the steady-state ensemble-averaged populations are $S : T_0 : T_+ : T_- = 2/9 : 7/27 : 7/27 : 7/27$, while in saturating magnetic field the ratios are $1/6 : 1/6 : 1/3 : 1/3$.

Supporting References

(1) Gadella, T. W. J.; Van Weeren, L.; Stouthamer, J.; Hink, M. A.; Wolters, A. H. G.; Giepmans, B. N. G.; Aumonier, S.; Dupuy, J.; Royant, A. mScarlet3: A Brilliant and Fast-Maturing Red Fluorescent Protein. *Nat Methods* **2023**, *20* (4), 541–545. https://doi.org/10.1038/s41592-023-01809-y.

(2) Bajar, B. T.; Wang, E. S.; Lam, A. J.; Kim, B. B.; Jacobs, C. L.; Howe, E. S.; Davidson, M. W.; Lin, M. Z.; Chu, J. Improving Brightness and Photostability of Green and Red Fluorescent Proteins for Live Cell Imaging and FRET Reporting. *Sci Rep* **2016**, *6* (1), 20889. https://doi.org/10.1038/srep20889.

(3) Legault, S.; Fraser-Halberg, D. P.; McAnelly, R. L.; Eason, M. G.; Thompson, M. C.; Chica, R. A. Generation of Bright Monomeric Red Fluorescent Proteins *via* Computational Design of Enhanced Chromophore Packing. *Chem. Sci.* **2022**, *13* (5), 1408–1418. https://doi.org/10.1039/D1SC05088E.

(4) Shcherbo, D.; Murphy, C. S.; Ermakova, G. V.; Solovieva, E. A.; Chepurnykh, T. V.; Shcheglov, A. S.; Verkhusha, V. V.; Pletnev, V. Z.; Hazelwood, K. L.; Roche, P. M.; Lukyanov, S.; Zaraisky, A. G.; Davidson, M. W.; Chudakov, D. M. Far-Red Fluorescent Tags for Protein Imaging in Living Tissues. *Biochemical Journal* **2009**, *418* (3), 567–574. https://doi.org/10.1042/BJ20081949.

(5) Guo, A. C.; Jewison, T.; Wilson, M.; Liu, Y.; Knox, C.; Djoumbou, Y.; Lo, P.; Mandal, R.; Krishnamurthy, R.; Wishart, D. S. ECMDB: The E. Coli Metabolome Database. *Nucleic Acids Research* **2012**, *41* (D1), D625–D630. https://doi.org/10.1093/nar/gks992.

(6) Sajed, T.; Marcu, A.; Ramirez, M.; Pon, A.; Guo, A. C.; Knox, C.; Wilson, M.; Grant, J. R.; Djoumbou, Y.; Wishart, D. S. ECMDB 2.0: A Richer Resource for Understanding the Biochemistry of *E. Coli*. *Nucleic Acids Res* **2016**, *44* (D1), D495–D501. https://doi.org/10.1093/nar/gkv1060.

(7) Holt, P. J.; Efremov, R. G.; Nakamaru-Ogiso, E.; Sazanov, L. A. Reversible FMN Dissociation from Escherichia Coli Respiratory Complex I. *Biochimica et Biophysica Acta (BBA) - Bioenergetics* **2016**, *1857* (11), 1777–1785. https://doi.org/10.1016/j.bbabio.2016.08.008.

(8) Hayashi, H.; Nagakura, S. Theoretical Study of Relaxation Mechanism in Magnetic Field Effects on Chemical Reactions. *Bulletin of the Chemical Society of Japan* **1984**, *57* (2), 322–328. https://doi.org/10.1246/bcsj.57.322.

(9) Murakami, M.; Maeda, K.; Arai, T. Dynamics of Intramolecular Electron Transfer Reaction of FAD Studied by Magnetic Field Effects on Transient Absorption Spectra. *J. Phys. Chem. A* **2005**, *109* (26), 5793–5800. https://doi.org/10.1021/jp0519722.

(10) Kattnig, D. R.; Evans, E. W.; Déjean, V.; Dodson, C. A.; Wallace, M. I.; Mackenzie, S. R.; Timmel, C. R.; Hore, P. J. Chemical Amplification of Magnetic Field Effects Relevant to Avian Magnetoreception. *Nature Chem* **2016**, *8* (4), 384–391. https://doi.org/10.1038/nchem.2447.

(11) Schulten, K.; Wolynes, P. G. Semiclassical Description of Electron Spin Motion in Radicals Including the Effect of Electron Hopping. *The Journal of Chemical Physics* **1978**, *68* (7), 3292–3297. https://doi.org/10.1063/1.436135.

(12) Cohen, A. E. Nanomagnetic Control of Intersystem Crossing. *J. Phys. Chem. A* **2009**, *113* (41), 11084–11092. https://doi.org/10.1021/jp907113p.